Materials Today Chemistry 45 (2025) 102661

Contents lists available at ScienceDirect

Materials Today Chemistry

journal homepage: www.journals.elsevier.com/materials-today-chemistry/

Synthesis-free swellable hydrogel microneedles for rapid interstitial fluid extraction and on-site glucose detection via an electrochemical biosensor system

Khaled Mohammed Saifullah [a,b], Pouria Azarikhah [a,b], Zahra Faraji Rad [a,b,*]

[a] School of Engineering, University of Southern Queensland, Queensland, 4300, Australia
[b] Centre for Future Materials, Institute for Advanced Engineering and Space Sciences, University of Southern Queensland, Queensland, Australia

ARTICLE INFO

Keywords:
Swellable microneedles
ISF
Skin applicator
Biomarker detection
Electrochemical biosensor
Glucose detection

ABSTRACT

Current methods to detect biomarkers often involve lengthy turnaround times due to the need for blood extraction and subsequent laboratory analysis. Microneedles (MNs) offer a minimally invasive solution to access the interstitial fluid (ISF); however, they are limited by challenges such as hazardous material synthesis, insertion techniques, small ISF volumes (2–5 μL), and lengthy extraction time. This study presents a novel swellable MN patch combined with a biosensing platform to enable on-site glucose detection through an optimized applicator-assisted insertion method. The highly efficient MN patch extracts up to 7.06 ± 0.44 μL of ISF in 5 min without the typical post-processing instruments such as vacuum or suction. The extracted ISF is applied to the modified electrodes, which detect the target biomarker (glucose) with high sensitivity (9.68 μA mM^{-1} cm^{-2}) and a low detection limit (0.08 mM) under optimized conditions. In addition to effectively recovering glucose molecules, the MN patch demonstrates enhanced efficiency and penetration depth, with a critical correlation established between the volume of extracted ISF and the glucose recovery rate, as validated through comprehensive *in-vitro* and *ex-vivo* tests. This MN-based biosensing approach could offer a viable alternative to traditional blood tests, glucometers, finger-prick methods, or continuous monitoring devices.

1. Introduction

ISF extraction using MNs has gained significant attention in recent years as an alternative to traditional methods for detecting a wide range of biomarkers or analytes, including glucose, for diabetes management. The human body holds more than three times the amount of ISF compared to blood, with 83 % of serum proteins commonly found in ISF, but 50 % of ISF proteins are unique and not found in blood, making it a convenient route for identifying both common and unique biomarkers [1–3]. Therefore, theoretically, it can be assumed that nearly all analytes present in the blood are also found in ISF, which is further supported by studies suggesting that 99 % of blood proteins are detectable via ISF [4–7]. While blood tests remain the gold standard for diagnostics, they require medical expertise and are invasive. In contrast, ISF extraction using MNs is minimally invasive as it accesses ISF near the skin's surface without requiring deep penetration into the skin tissue, alleviating the needle phobia and avoiding the clotting concerns typically associated with blood draws [2,5].

Although the development of MNs for ISF extraction and biosensing has progressed rapidly, several challenges remain. One of the most critical hurdles is ensuring the extraction of sufficient volumes of ISF (>5 μL) consistently and rapidly (>5 min). While fast extraction of ISF is attempted, the success of MN-based ISF extraction largely depends on the swelling capacity of the MN materials, their mechanical strength, and the insertion efficiency. Optimizing these factors is necessary to ensure reliable skin penetration and maximum ISF uptake. Compared to other MN types (e.g., solid and hollow), swellable MNs offer the advantage of absorbing ISF directly upon insertion, simplifying the extraction process. Various materials have been explored to improve the performance of swellable MNs; however, they often involve complex synthesis processes, extended extraction times, additional post-insertion methods (e.g., vacuum or negative pressure) or limited by sampling volumes [4,8–20].

This study introduces a novel synthesis-free, applicator-assisted spiral MN patch to rapidly extract ISF and direct on-site glucose detection using an electrochemical biosensor. The spiral design of the MN is

* Corresponding author. School of Engineering, University of Southern Queensland, Queensland, 4300, Australia.
E-mail address: zahra.farajirad@unisq.edu.au (Z. Faraji Rad).

https://doi.org/10.1016/j.mtchem.2025.102661
Received 6 January 2025; Received in revised form 21 March 2025; Accepted 21 March 2025
Available online 2 April 2025

chosen for its ability to provide enhanced interlocking capabilities, ensuring that the MNs remain securely inserted in the skin during ISF extraction. MNs are developed from gelatin/PVA with varying concentrations of osmolyte (maltose) and powered by super absorbent polymer (SAP) for rapid swelling. The maltose incorporated into the MN formulations creates a strong osmotic gradient that helps to draw ISF into the MNs, while the SAP ensures that the MNs swell quickly without compromising their structural integrity.

To facilitate the insertion of the MNs, a custom-designed applicator system is developed based on our previous study [21,22], which can apply a controlled velocity of 4.5 m s^{-1} and vibration of 100 Hz to enhance penetration through the skin. To validate the insertion methods and capabilities of the MNs, a series of *in-vitro* and *ex-vivo* tests are conducted using artificial ISF (aISF) or ISF. Three different MN insertion methods (e.g., manual pressed, applicator-assisted, and vibration-assisted) are tested and compared based on ISF uptake, insertion efficiency, depth and recovery, aiming to identify the most effective technique for maximizing ISF extraction. Using the applicator system makes the insertion process standardized, reducing variability associated with manual techniques and minimizing user errors.

In addition, the study also proposes an electrochemical biosensor based on the screen-printed electrodes (SPEs) capable of detecting glucose levels directly from the extracted aISF. The optimized biosensor's ability to detect glucose at various concentrations is validated using chronoamperometry, and its selectivity is tested in the presence of common interferents. The SPEs are modified with Prussian blue (PB) as a mediator and glucose oxidase (GO_x) as the enzyme responsible for catalyzing glucose oxidation. Single-walled carbon nanotubes (SWCNTs) and Nafion were incorporated to improve enzyme immobilization, electron transfer, and selectivity.

This study bridges the gap between the need for efficient ISF extraction and on-site glucose detection by introducing a novel MN-based sensing platform that leverages osmolyte-driven fluid uptake and electrochemical sensing technology. Through the extraction of ISF using advanced swellable hydrogels and applicator-assisted engineering techniques, this MN platform develops a user-friendly and minimally invasive approach with the possibility of extending beyond diabetes management to include the detection of other biomarkers in ISF (Fig. 1).

2. Results and discussion

2.1. Fabrication and morphology of the spiral MNs

MNs were designed in a spiral shape with tapered tips to provide interlocking capabilities which come from the number of vertices (or turns) in the spiral that create greater resistance during retraction due to increased friction, adhesion, and mechanical entanglement with the tissue matrix (Fig. S1). The CAD design of the MNs had a height of 1000 μm with a base diameter of 300 μm to ensure minimally invasive insertion and sufficient extraction of ISF from the skin [7,23]. The distance between the needle tip-to-tips was designed to be 700 μm to reduce needle compactness, which could impact insertion ability [23,24]. The base thickness of the patch was set to 1500 μm.

For printing, the CAD file was converted to STL file format and printed using a microArch® S240 ultra-high-resolution 3D printer (Boston Microfabrication, MA, USA) on a biocompatible high-performance silicone castable resin (High-Temperature Liquid, HTL) with a tensile strength of 79.3 MPa, a heat deflection temperature (HDT) of 114 °C, and a glass transition temperature (T_g) of 172 °C. Projection Micro Stereolithography (PμSL) technique was used for printing the MNs by projecting a focused light beam onto the photosensitive resin, which underwent polymeric crosslinking and solidification following exposure to light. This layer-by-layer approach built the entire spiral structure with a resolution of 2 μm, which was then used to create PDMS negative molds using the micro-molding technique. For replication, the molds were filled with the prepared solution and dried for 36 h at room temperature to form the swellable MN patches (Fig. 2a). For simplicity, each MN patch is denoted as MN-MalX, where 'MN' is the combination of gelatin/PVA (6/4, w/v), 'Mal' refers to added maltose, and 'X' indicates the maltose concentration (e.g., MN-Mal0 has no maltose, MN-Mal3 has 3 %, w/v, and MN-Mal5 has 5 %, w/v). The detailed geometry of the MNs and the 3D printing process is shown in Fig. S2.

High-resolution SEM imaging was used to capture the fine spiral structure, uniform spacing and sharp tips of the MNs (Fig. 2b). Although PμSL offers high-fidelity printing between the CAD design and the produced 3D object, printing the MN patch resulted in dimensional deviations from the original CAD file. For example, the actual height of the MNs was less than the initial design. The longitudinal shrinkages from the original design (1000 μm) for MN-Mal0, MN-Mal3, and MN-Mal5 were ≈31.62 %, ≈32.52 %, and ≈32.24 %, respectively (Fig. 2c). The shrinkage difference between the swellable MNs was not statistically

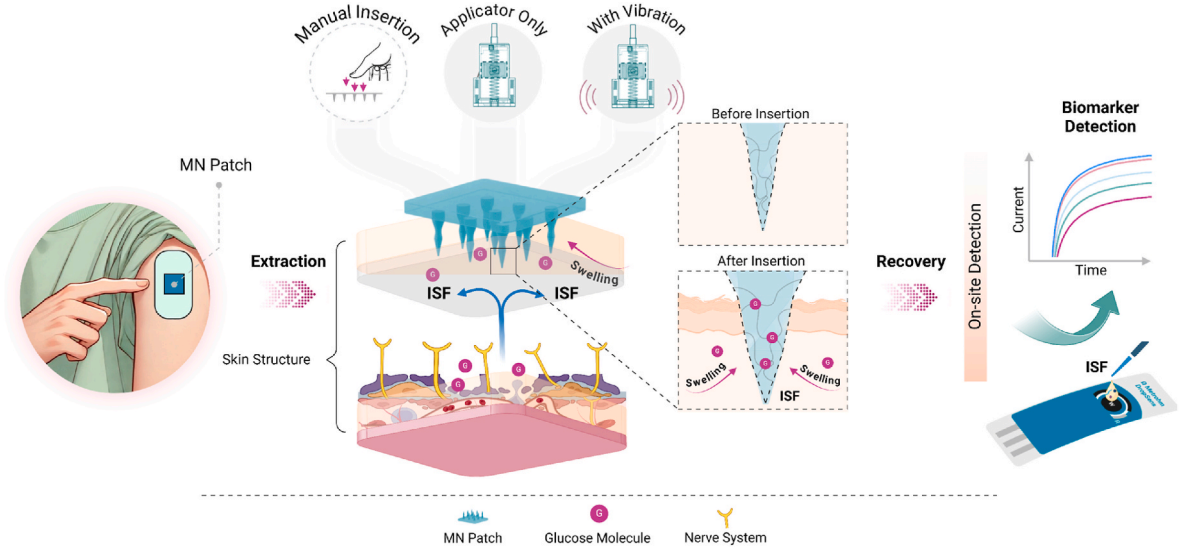

Fig. 1. Schematic illustration of spiral MNs using three different insertion techniques to rapidly extract ISF through the swelling mechanism of the MNs and recover glucose for on-site detection via SPEs.

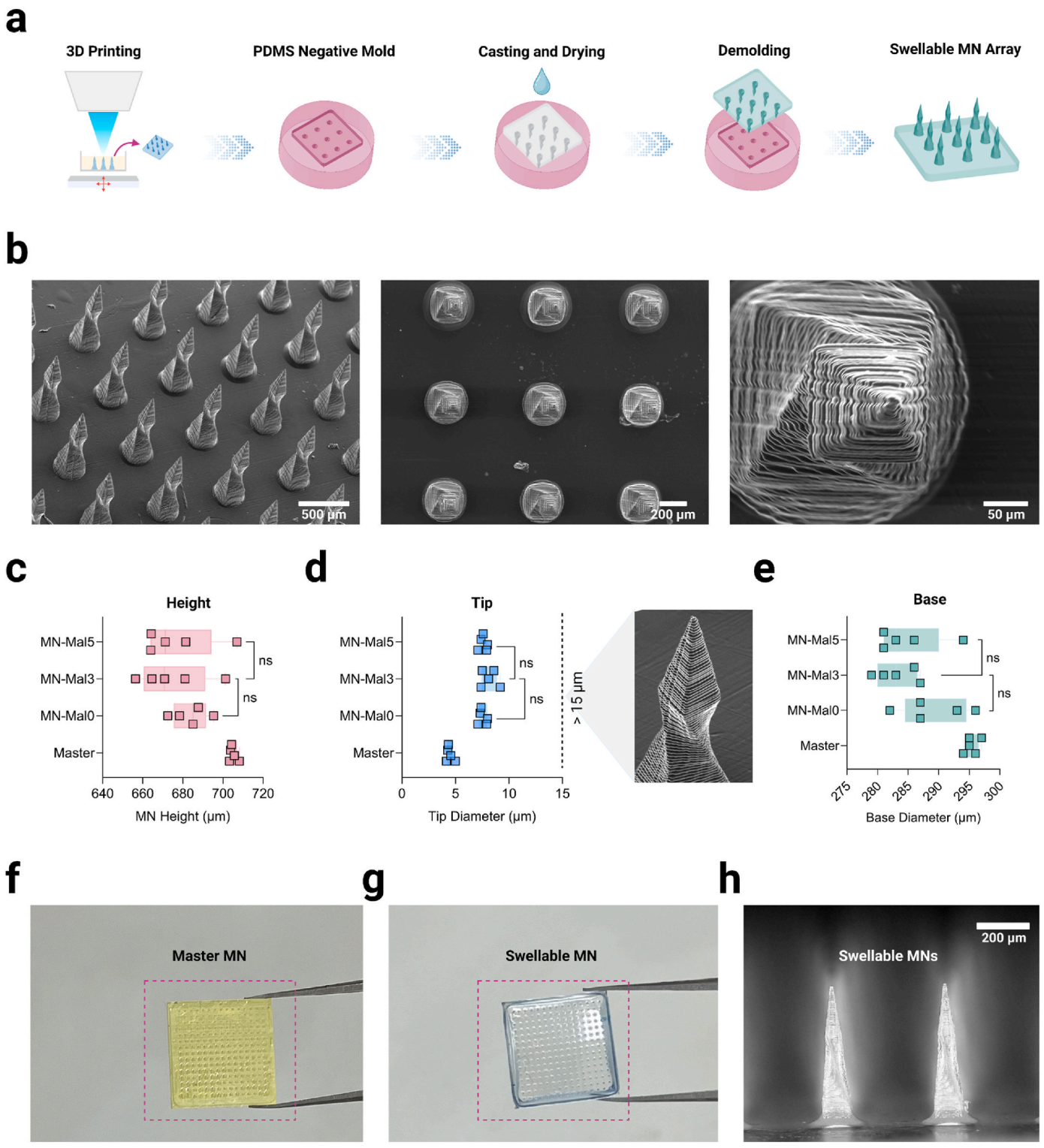

Fig. 2. Fabrication, characterization, and morphological analysis of swellable MNs. a) Schematic representation of the fabrication process, including 3D printing of master MNs, PDMS mold preparation, casting, drying, demolding, and replication of the final MN patch. b) SEM images of the MNs at different magnifications, showing the complex structure in detail c) Comparison of MNs shrinkage in heights between different formulations (Swellable MN-Mal0, MN-Mal3, MN-Mal5) and the master MN. d) Comparison of MN tip diameter between MN master and different formulations (MN-Mal0, MN-Mal3, MN-Mal5) of the swellable MNs. e) Base diameter comparison between master MN and different formulations (MN-Mal0, MN-Mal3, MN-Mal5). f) An image of the Master MN patch (15 × 15) with a square base. g) An image of the swellable MN patch (15 × 15) with a transparent morphology. h) Optical microscopic image of the swellable MNs showing identical morphology between the needles.

significant ($p \geq 0.05$, $n = 5$). Tip diameter of the MNs can play a crucial role in insertion, as smaller tips enable smoother and more efficient skin penetration [25]. Master MNs produced by 3D printing had the sharpest tip with a diameter of ≈4.47 μm. Swellable MNs' tip diameter was ≈7.54 μm (MN-Mal0), ≈8.16 μm (MN-Mal3) and ≈7.6 μm (MN-Mal5) respectively, as shown in Fig. 2d (left). SEM image of the upper part of a single MN tapering to a sharp tip (>15 μm) is also highlighted with a close-up view in Fig. 2d (right). The difference in tip diameters between the swellable MNs was also not statistically significant ($p \geq 0.05$, $n = 5$) and well below the recommended tip diameter of 15 μm for effective skin penetration [25]. The measured base diameters were slightly reduced from the original CAD design (300 μm) across the different MN types. For example, the base diameter of the master MN was 295.40 ± 1.14 μm, and for MN-Mal0, MN-Mal3, and MN-Mal5, the base diameters were 289 ± 5.52 μm, 283.20 ± 3.35 μm, and 285 ± 5.43 μm, respectively (Fig. 2e). The captured images showing the MN patch (15 × 15) remained identical across both the master and fabricated design (Fig. 2f and g), while optical images of the swellable MNs are shown in Fig. 2h.

2.2. Swelling and mechanical characteristics of MNs

Swelling behavior and mechanical properties of the MNs are among the most important aspects in extracting a higher volume of ISF. Generally, excessive MN swelling can reduce mechanical strength, while higher mechanical strength can compromise swelling. Therefore, finding an optimal balance between them is important so they do not overlap significantly. To achieve this balance, the swelling properties of the MN material were optimized (Fig. S3) by adjusting the concentrations of gelatin/PVA and maltose with the MNs replicated from the master template using negative molds. MN patches were then tested in aISF to determine the swelling properties. Rapid swelling was observed over time due to the presence of SAP and osmolyte in the hydrogel structure. After 5 min, the swelling ratio for MN-Mal0, MN-Mal3, and MN-Mal5 reached 467 ± 49.41 %, 561 ± 48.04 %, and 596 ± 23.59 %, respectively (Fig. 3a). SAP has an exceptionally high capacity for water absorbency; hence, combined with osmolytes (maltose) and polymers (gelatin and PVA), the swellable MNs could rapidly transition from a dry to a swollen state without being dissolved. In contrast, MNs made without SAP (PAA-Na) gradually disintegrated within the first 5 min of the test, and the shape of the MNs was not visible. The results suggested that adding SAP and osmolyte (maltose) in MNs significantly enhanced the swelling capacity and maintained their structural integrity. This allowed the MNs to maintain their functionality during the swelling test and enhanced stability to prevent premature disintegration. Although MNs could continue swelling until they reached equilibrium, ISF extraction beyond 5 min was impractical, and further swelling was not considered. This is because the extraction time and ability of MNs directly depend on their ability to swell. Fast swelling is the most important aspect, as it minimizes the time required for sample collection and makes the process more feasible for frequent and on-site biomarker detection. Optical images of the MNs revealed a substantial increase in size upon swelling while remaining reasonably intact (Fig. 3b).

The mechanical strength of MNs is another crucial factor as it ensures that MNs can penetrate the skin successfully. Therefore, a compressive

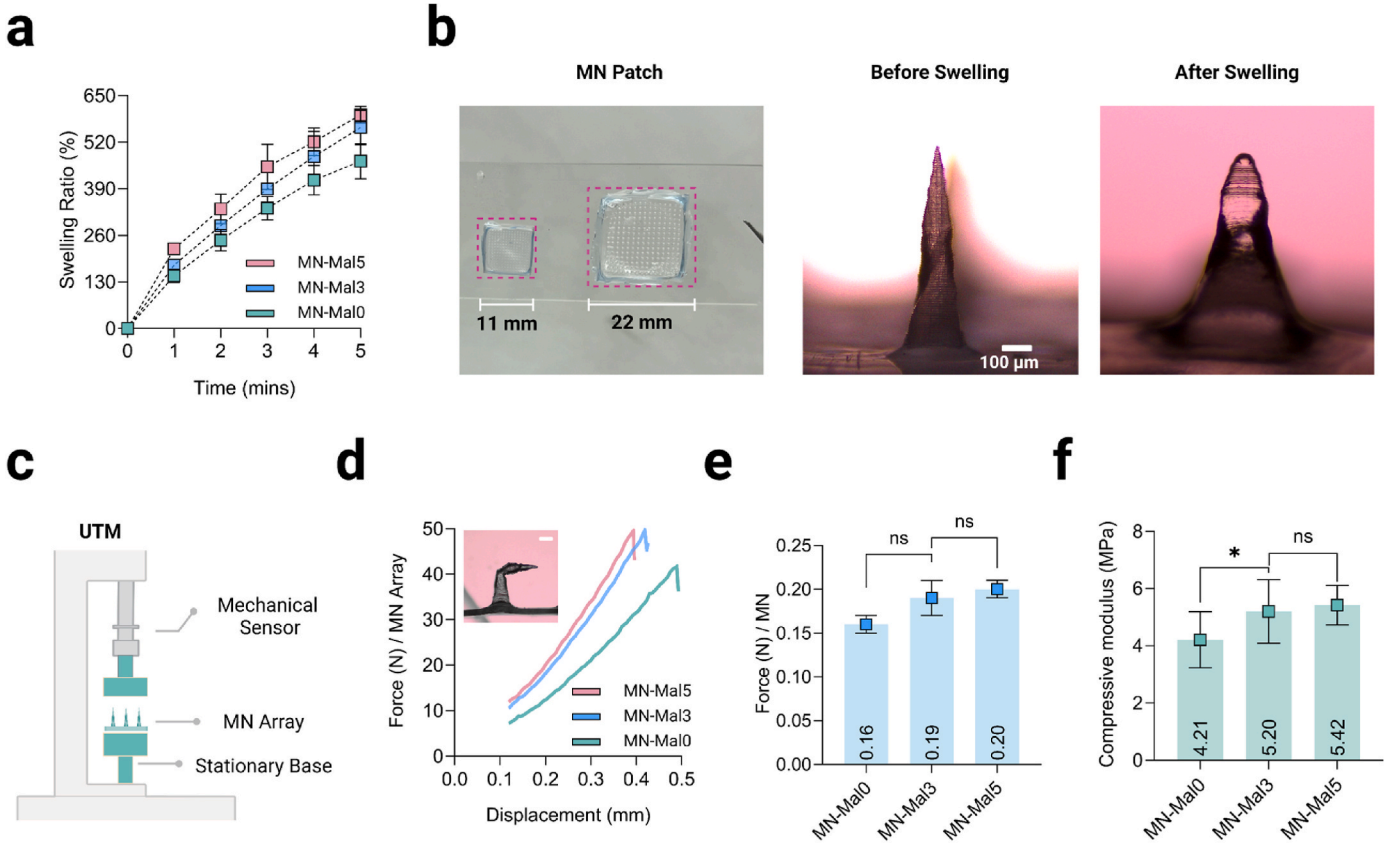

Fig. 3. Swelling and mechanical properties of the MNs replica. a) Swelling ratio (%) of the MN-Mal0, MN-Mal3, and MN-Mal5 over 5 min, indicating that all formulations exhibit increased swelling, with MN-Mal5 showing the highest swelling ratio. b) Optical and captured images of MNs before and after swelling showing morphological change in shape and size. c) Schematic illustration of the setup for mechanical testing of the MN patch, with a mechanical sensor applying force to the MNs mounted on a stationary base. d) Force (N) versus displacement (mm) curve of MN-Mal0, MN-Mal3, and MN-Mal5, showing differences in mechanical strength across all formulations. The inset shows the post-impact image of a single MN (Scale bar: 100 μm). e) Maximum force (N) each MN can withstand, showing no significant difference between all formulations. f) Compressive modulus (MPa) of the MN-Mal0, MN-Mal3, and MN-Mal5, with MN-Mal5 showing improved strength than the other two formulations.

load test was conducted to assess the mechanical strength of the MNs. MN patches were placed between the plates of the test instrument equipped with a mechanical sensor to obtain the force versus displacement curve (Fig. 3c). As the movable upper plate touched the tip of the MN, the force increased to a peak before dropping and then approaching a second peak. The first peak, the failure load, confirmed the permanent deformation of the MNs in a vertical direction without any fragmentation (Fig. 3d). The failure mode was primarily bending, with no noticeable torsion or twisting at the point of failure. The fracture force for each patch of MN-Mal0, MN-Mal3, and MN-Mal5 was 36.23 N, 43.04 N, and 46.86 N, respectively. For a single MN, the forces were about 0.16 N, 0.19 N, and 0.20 N with no statistical significance ($p \geq 0.05$, $n = 5$), respectively (Fig. 3e), which are about 1.7, 2.2, and 2.4 times higher than the required force to penetrate the skin (0.058 N) [23], indicating that the replicated MNs possess enough strength to penetrate the skin without fracture. This was further supported by the compressive modulus of MN-Mal0, MN-Mal3, and MN-Mal5 measured at ≈ 4.21 MPa, ≈5.20 MPa, and ≈5.42 MPa, respectively (Fig. 3f), with MN-Mal0 and MN-Mal3 indicated statistical significance in results ($p < 0.05$, $n = 5$). This suggested that adding osmolytes (maltose) can also influence the mechanical strength of the MNs. For instance, MNs without maltose (MN-Mal0) had 15.78 % (MN-Mal3) and 20 % (MN-Mal5) lower mechanical strength compared to those with maltose. The presence of maltose created osmotic pressure that also aided the fluid uptake. Conversely, the results showed that further increasing the concentration of osmolytes (≥7 %, w/v) made the MNs brittle and reduced their swelling behavior (Fig. S3). This could be due to the structural change altering the properties of SAP by occupying a significant portion of the hydrogel matrix, making it less porous. In contrast, the presence of SAP with the optimal amount of osmolytes balanced the swelling and mechanical properties of the MNs to an ideal state when combined with a hydrogel matrix (gelatin and PVA) without the need for additional cross-linkers (e.g., glutaraldehyde) or synthetization (e.g., gelatin methacryloyl, GelMA).

Various studies have demonstrated good swelling and mechanical properties using different hydrogel compositions. One such study by Zhu et al. reported a crosslinked GelMA MN patch capable of swelling up to 410 ± 79 % within the first 10 min in DPBS solution, with a compressive modulus of 5.80 MPa [8]. Xu et al. developed a MN patch composed of PVA and polyvinylpyrrolidone (PVP) that swelled by ≈ 450 % in PBS within 12 min while maintaining the structural integrity of the tip [26]. He et al. reported another hydrogel MN patch made of PVA and chitosan (CS) demonstrated swelling of 850 % in 30 min with a fracture force greater than 3 N/needle [10]. Qiao et al. demonstrated that a MN patch consisting of crosslinked GelMA and graphene oxide (GO) would swell up to 383.58 % in 30 min with a fracture force of 0.22 N/needle [11]. A different study by Fonseca et al. reported a hydrogel MN patch capable of swelling up to 201 ± 4 % in 20 min, with each needle able to withstand a force of 0.30 ± 0.03 N [27]. Compared to previous studies, MN patches developed in this study showed improved swelling and balanced mechanical strength for rapid extraction of ISF. A comparative summary table of the swelling properties of the MNs and their mechanical strength is provided in Table S1.

2.3. Insertion and extraction capabilities of MNs with and without applicator

One of the most significant challenges for successful MN penetration is overcoming the stratum corneum (SC), the primary barrier to substances entering the body [28,29]. Therefore, three different insertion techniques: manual insertion (thumb press), applicator only (0 Hz, 4.5 m s^{-1}) and applicator with vibration (100 Hz, 4.5 m s^{-1}) were explored for successful insertion, penetration, and extraction capabilities of the MNs [21,22].

Initially, insertion tests were conducted by stacking eight layers of Parafilm (127 μm each, total thickness ≈ 1 mm) to mimic the elastic properties of skin [30]. MNs were applied to the Parafilm manually and with the applicator (0 Hz and 100 Hz, 4.5 m s^{-1}), which resulted in a uniform pattern of micro-holes on different layers. The first layer of the Parafilm is the most important as it acts as the SC where MN failure predominantly occurs. After the insertion, the imprint from the MN patch was clearly visible on the Parafilm (Fig. 4a), and the efficiency was calculated based on the number of holes successfully pierced through the Parafilm. The results demonstrated noticeable improvement in the applicator-assisted method compared to manual insertion. For MN-Mal0, the efficiency for manual insertion was about ≈77.16 %, which increased to ≈95.58 % (0 Hz, 4.5 m s^{-1}) and ≈95.47 % (100 Hz, 4.5 m s^{-1}) with the applicator. MN-Mal3 showed similar results, with an efficiency of about ≈84.09 % for manual application, improving to ≈96.18 % (4.5 m s^{-1}) and ≈96.62 % (100 Hz, 4.5 m s^{-1}) using the applicator. MN-Mal5 demonstrated the highest penetration efficiency with the manual insertion at ≈ 86.22 %, improving to about ≈97.44 % (0 Hz, 4.5 m s^{-1}) and ≈97.60 % (100 Hz, 4.5 m s^{-1}) by the applicator. The results showed that efficiency increased with the applicator-assisted insertion, with the improvements being statistically significant ($p < 0.05$ and $p < 0.01$, $n = 5$) (Fig. 4b). The difference between the applicator without vibration (0 Hz, 4.5 m s^{-1}) and with vibration (100 Hz, 4.5 m s^{-1}) was not statistically significant ($p > 0.05$, $n = 5$). Noticeable improvements were also observed in penetration depth using the applicator insertion method (Fig. 4c). In the case of manual insertion (thumb press), the MN-Mal0 penetration depth was 195.16 ± 20.05 μm, which increased to 275.55 ± 22.08 μm (0 Hz, 4.5 m s^{-1}) and 284.25 ± 20.09 μm (100 Hz, 4.5 m s^{-1}) with the use of applicator. A similar improvement trend was noticed for MN-Mal3, with the penetration depth increasing from 274.02 ± 43.19 μm (manual insertion) to 311.60 ± 12.67 μm (0 Hz, 4.5 m s^{-1}) and 317.99 ± 8.86 μm (100 Hz, 4.5 m s^{-1}) with the applicator. For MN-Mal5, the manual insertion depth was 280.10 ± 48.07 μm, increasing to 334.51 ± 21.54 μm (0 Hz, 4.5 m s^{-1}) and 335.51 ± 21.82 μm (100 Hz, 4.5 m s^{-1}) with the applicator. The improvements over the applicator without vibration (4.5 m s^{-1}) are only about 3 % (MN-Mal0) and 2 % (MN-Mal3), while MN-Mal5 showed almost no improvement ($p > 0.05$, $n = 5$) (Fig. 4d). Noticeably, in the second layer, the diameters of the micro-holes were reduced, and a significant decrease was observed in the third layer, with no holes visible in the fourth. Since each parafilm layer is ≈ 127 μm thick, the maximum theoretical MN penetration depth was ≈381 μm (equivalent to three layers of Parafilm), which is ≈ 36 % (manual), ≈13.8 % (0 Hz, 4.5 m s^{-1}) and 13.55 % (100 Hz, 4.5 m s^{-1}) higher for MN-Mal5. This is likely because the theoretical calculations assume uniform penetration through each layer but do not fully account for micro-level variations in the third layer during actual penetration.

To further explore the ISF uptake, insertion efficiency, and depth of MNs, they were manually inserted into 1.4 % (w/v) agarose gel prepared in aISF for 5 min (Fig. 4e). The swelling ability and holes created by the MNs were subsequently analyzed. Upon insertion into the agarose gel, the MNs began to swell due to the aISF, extracting 9.09 ± 1.25 μL, 11.14 ± 1.15 μL, and 12.49 ± 1.26 μL for MN-Mal0, MN-Mal3, and MN-Mal5, respectively, in 5 min (Fig. 4f). This is due to osmolytes creating higher osmotic pressure within the MNs compared to the aISF in the agarose gel. Therefore, an increase in the concentration of maltose exhibited higher ISF extraction ability. Zheng et al. also reported that incorporating osmolyte-like maltose in methacrylated hyaluronic acid (MeHA) MNs enhances ISF extraction [12]. Penetration efficiency was 98.04 ± 0.24 %, 98.13 ± 0.58 %, and 98.31 ± 0.58 % for MN-Mal0, MN-Mal3, and MN-Mal5, respectively (Fig. 4g). Penetration depths into the agarose gel were 620.88 ± 12.26 μm, 634.35 ± 35.75 μm, and 643.25 ± 20.32 μm for MN-Mal0, MN-Mal3, and MN-Mal5, respectively (Fig. 4h). The applicator-assisted insertion was not used in the agarose gel test because the insertion (0–100 Hz, 4.5 m s^{-1}) could pierce through the gel too quickly, compromising the ability to observe the controlled penetration and extraction behavior of the MNs.

In addition to the manual insertion technique used in the agarose gel

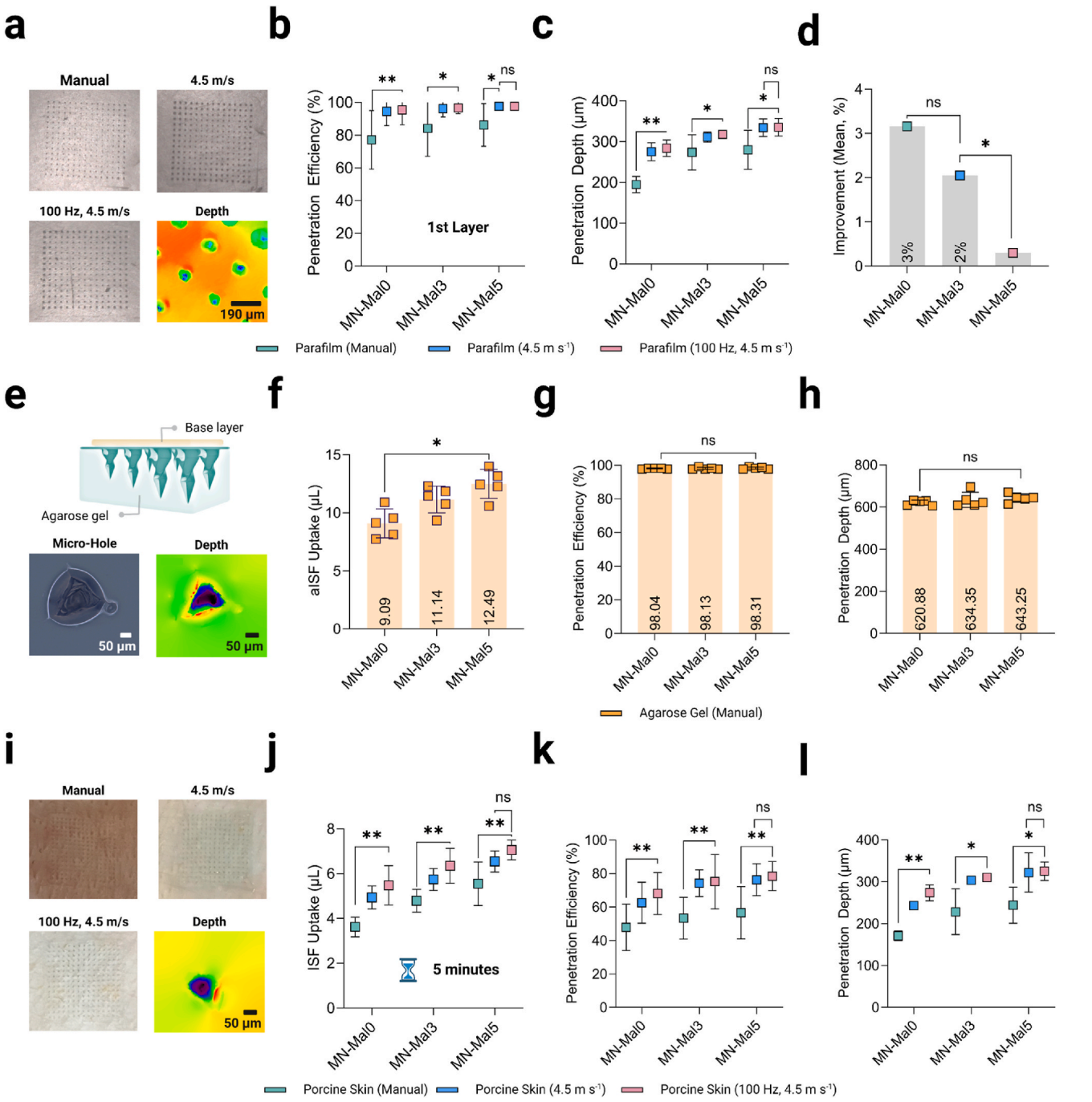

Fig. 4. Performance of the swellable MNs in terms of ISF/aISF uptake, penetration efficiency, and depth across three insertion techniques – manual, applicator without vibration (0 Hz, 4.5 m s^{-1}), and applicator with vibration (100 Hz, 4.5 m s^{-1}). a) Visual images of micro-holes on parafilm left by the MN patch after manual insertion, applicator without vibration (0 Hz, 4.5 m s^{-1}), and applicator with vibration (100 Hz, 4.5 m s^{-1}) for MN-Mal0, MN-Mal3, and MN-Mal5. b) Penetration efficiency (%) of the first layer of parafilm using manual insertion, applicator without vibration (4.5 m s^{-1}), and applicator with vibration (100 Hz, 4.5 m s^{-1}) for MN-Mal0, MN-Mal3, and MN-Mal5. c) Penetration depth (µm) into parafilm for manual insertion, applicator without vibration (0 Hz, 4.5 m s^{-1}), and applicator with vibration (100 Hz, 4.5 m s^{-1}) across MN-Mal0, MN-Mal3, and MN-Mal5. d) Mean percentage improvement with vibration (100 Hz, 4.5 m s^{-1}) over no vibration for MN-Mal0, MN-Mal3, and MN-Mal5. e) Schematic and optical images showing the micro-holes created in agarose gel after MN insertion, with corresponding depth profile visualized. f) aISF uptake (µL) from agarose gel using manual insertion for MN-Mal0, MN-Mal3, and MN-Mal5. g) aISF uptake (µL) from agarose gel using manual insertion for MN-Mal0, MN-Mal3, and MN-Mal5. g) Penetration efficiency (%) on the agarose gel using manual insertion for MN-Mal0, MN-Mal3, and MN-Mal5. h) Penetration depth (%) on the agarose gel using manual insertion for MN-Mal0, MN-Mal3, and MN-Mal5. i) Visual and optical images of micro-holes on porcine skin left by the MN patch with corresponding depth profile visualized post manual insertion, applicator without vibration (0 Hz, 4.5 m s^{-1}), and applicator with vibration (100 Hz, 4.5 m s^{-1}) for MN-Mal0, MN-Mal3, and MN-Mal5. j) ISF uptake (µL) from the porcine skin using manual insertion, applicator without vibration (0 Hz, 4.5 m s^{-1}), and applicator with vibration (100 Hz, 4.5 m s^{-1}) for MN-Mal0, MN-Mal3, and MN-Mal5. k) Penetration efficiency (%) on the porcine skin using manual insertion, applicator without vibration (0 Hz, 4.5 m s^{-1}), and applicator with vibration (100 Hz, 4.5 m s^{-1}) for MN-Mal0, MN-Mal3, and MN-Mal5. i) Penetration depth (%) on the agarose gel using manual insertion, applicator without vibration (0 Hz, 4.5 m s^{-1}), and applicator with vibration (100 Hz, 4.5 m s^{-1}) for MN-Mal0, MN-Mal3, and MN-Mal5.

test, MN patches were further applied to fresh porcine skin manually and with an applicator assisted with (100 Hz, 4.5 m s^{-1}) and without vibration (0 Hz, 4.5 m s^{-1}) (Fig. 4i). Following the application, successful penetration was confirmed by the micro-holes visible on the porcine skin placed on a non-slip surface. However, manual insertion of the MNs into porcine skin resulted in the lowest outcomes across all measured parameters. For example, only 3.62 ± 0.44 μL, 4.79 ± 0.51 μL, and 5.55 ± 0.97 μL of ISF were extracted by MN-Mal0, MN-Mal3, and MN-Mal5, respectively (Fig. 4j). The penetration efficiencies were 47.91 ± 13.83 %, 53.33 ± 12.43 % and 56.62 ± 15.60 % for MN-Mal0, MN-Mal3, and MN-Mal5, respectively (Fig. 4k). Penetration depths showed similar results at 171.19 ± 11.61 μm, 228.50 ± 54.50 μm, and 244.10 ± 42.95 μm for MN-Mal0, MN-Mal3, and MN-Mal5, respectively (Fig. 4l).

The applicator effectively improved the insertion and extraction capabilities of the MNs. With the applicator-assisted insertion (0 Hz, 4.5 m s^{-1}), 4.94 ± 0.51 μL, 5.74 ± 0.49 μL, and 6.55 ± 0.47 μL of ISF was extracted by MN-Mal0, MN-Mal3, and MN-Mal5, respectively (Fig. 4j). ISF uptake increased by about 36.46 %, 19.83 %, and 18 % compared to manual insertion on the *ex-vivo* skin for MN-Mal0, MN-Mal3, and MN-Mal5, respectively. Additionally, penetration efficiency was 62.58 ± 12.18 %, 74.22 ± 7.99 %, and 76.27 ± 9.59 % for MN-Mal0, MN-Mal3, and MN-Mal5, respectively (Fig. 4k), further reflecting improvements of about 30.62 %, 39.16 %, and 34.70 % compared to manual insertion. Furthermore, penetration depth was also enhanced to 243 ± 6.75 μm, 303.79 ± 8.25 μm, and 322.15 ± 46.82 μm for MN-Mal0, MN-Mal3, and MN-Mal5, respectively (Fig. 4l). This indicates an improvement in penetration depth of 41.95 %, 32.95 %, and 31.97 % over manual insertion.

Next, MNs were applied using the applicator with vibration (100 Hz, 4.5 m s^{-1}). After 5 min, 5.48 ± 0.87 μL, 6.35 ± 0.78 μL, and 7.06 ± 0.44 μL of ISF were extracted by MN-Mal0, MN-Mal3, and MN-Mal5, respectively (Fig. 4j), showing improvements of around 51.27 %, 32.57 %, and 27.14 % compared to manual insertion. Penetration efficiency of the MNs was 68.09 ± 12.46 %, 75.20 ± 16.22 %, and 78.49 ± 8.71 % for MN-Mal0, MN-Mal3, and MN-Mal5, respectively, indicating improvement of about 42.12 %, 41.00 %, and 38.62 % over manual insertion. (Fig. 4k). Penetration depths increased significantly to 273.86 ± 18.96 μm, 310.14 ± 7.77 μm, and 325.45 ± 21.93 μm for MN-Mal0, MN-Mal3, and MN-Mal5, respectively (Fig. 4l). The result indicated an improvement of about 59.98 %, 35.73 %, and 33.33 % compared to manual insertion.

The findings revealed that vibration (100 Hz, 4.5 m s^{-1}) during insertion can enhance the overall penetration depth and extraction capabilities of the MNs, particularly for MNs with lower mechanical strength. For example, applicator with vibration (100 Hz, 4.5 m s^{-1}) improved ISF uptake by approximately 10.94 % (MN-Mal0), 10.63 % (MN-Mal3), and 7.79 % (MN-Mal5), Penetration depth was also improved about 12.70 % (MN-Mal0), 2.09 % (MN-Mal3), and 1.02 % (MN-Mal5), while the efficiency increased by 8.81 % (MN-Mal0), 1.32 % (MN-Mal3), and 2.92 % (MN-Mal5) compared to the applicator without vibration (0 Hz, 4.5 m s^{-1}). However, insertion and extraction ability also depend on the swelling of the polymer matrix. Additionally, mechanical strength, penetration depth, and efficiency are interdependent. For example, MNs with lower mechanical strength will likely have reduced penetration depth and efficiency, resulting in decreased ISF uptake, even if the MNs are highly swellable. Thus, MNs with the lowest mechanical strength and swelling capacity (MN-Mal0) showed the greatest improvement with the vibration-assisted applicator across all aspects (swelling, depth, and efficiency). The results showed that MN-Mal0 insertion and extraction are more effective with the applicator, offering better precision and consistency. MNs with better mechanical properties and swelling capabilities (MN-Mal3 and MN-Mal5) can also benefit from the applicator, though the impact was less significant between the applicator with and without vibration. A comparative summary table of the above three insertion tests is provided in Table S2.

The performance of MNs on porcine skin exhibited significant differences in ISF uptake, penetration depth, and efficiency compared to the agarose gel test. The porcine skin test results were closely aligned with those obtained from the Parafilm test. For example, penetration depths observed on porcine skin were only about 3.65 %, 2.46 %, and 3 % lower than those recorded on Parafilm with the same settings (100 Hz, 4.5 m s^{-1}). This could be attributed to the Parafilm's ability to closely replicate the mechanical properties of skin, such as resistance and elasticity, resulting in similar MN performance. In contrast, agarose gel offers a more uniform density and reduced elasticity, facilitating easier penetration and higher ISF uptake.

Numerous studies have investigated different material compositions to enhance the aISF/ISF uptake of MNs. For instance, *Zhu* et al. reported a MN patch (*GelMA*) that extracted ≈ 2.5 μL of ISF in 10 min *in vivo* [8]. Similarly, *Xu* et al. developed a MN patch (*PVA/PVP*) that extracted ≈ 4.4 μL of ISF in 12 min in an *in vivo* setting [26]. *He* et al. introduced another hydrogel MN patch (*PVA/CS*) capable of extracting 7.5 μL of ISF in just 6 min [10], while *Qiao* et al. developed a MN patch (*GelMA/-graphene oxide*) that extracted 21.34 μL of ISF in 30 min *in vitro* [11]. Additionally, *Fonseca* et al. reported a MN patch (*crosslinked-GelMA*) that extracted 3.0 ± 0.7 μL of ISF in 30 min from human abdominal *ex vivo* skin [27]. *Zheng* et al. reported a MN patch (*methacrylated hyaluronic acid and maltose*) that extracted 3.82 μL of ISF from mice skin *in vivo* in 3 min [12], while *Laszlo* et al. demonstrated an acrylate-based MN patch that could extract 6 μL of dermal ISF in 10 min *in vivo* [13]. Furthermore, *Chang* et al. studied a MN patch (methacrylate hyaluronic acid) that extracted 2.3 ± 0.4 μL of ISF in 10 min from an *in vivo* mouse model [14]. Compared to these existing studies, the swellable MN-Mal5 patch showed improved ISF extraction, exceeding 5 μL within just 5 min. This is due to the unique combination of SAP and osmolyte-like maltose in the MN formulation, which not only enhances swelling capacity but also improves mechanical integrity during skin penetration. Additionally, the optimized insertion techniques, such as the applicator-assisted method, further improved the efficiency of ISF extraction. A comparative summary table of ISF extraction, volume, and time compared with other studies is provided in Table S3.

2.4. Recovery of glucose in in-vitro and ex-vivo models

To assess the ability of MNs to recover glucose, experiments were conducted using three models: aISF, agarose gel, and porcine skin. MN patches were heated, vortexed, and centrifuged to dissolve, after which glucose concentrations were measured. The recovery rates were determined by comparing the measured glucose concentrations with known concentrations ranging from 5 mM to 30 mM (Fig. 5a).

The results suggest the recovery rate was the highest in the aISF solution, recovering 75.13 ± 5.27 %, 79.42 ± 7.78 % and 80.07 ± 6.12 % of glucose from MN-Mal0 MN-Mal3 and MN-Mal5, respectively. The MNs tested on the agarose gel model showed slightly lower recovery rates of 73.19 ± 7.27 %, 76.49 ± 8.02 %, and 77.73 ± 7.11 % for MN-Mal0, MN-Mal3, and MN-Mal5, respectively (Fig. 5b). This reduction may be attributed to the denser matrix of the agarose gel and the fact that MNs were only inserted rather than fully submerged. In the porcine skin model (pre-soaked overnight in varying glucose concentrations), the recovery rate of the MNs was 40.23 ± 4.05 %, 45.29 ± 2.41 %, and 46.37 ± 7.62 % for MN-Mal0, MN-Mal3, and MN-Mal5, respectively (Fig. 5c). This could be due to reduced ISF volume, lower penetration depth, and decreased efficiency in accessing glucose molecules within the skin. However, with the applicator (0 Hz, 4.5 m s^{-1}), the recovery rates improved to 62.29 ± 9.25 %, 65.99 ± 10.33 %, and 67.95 ± 7.68 % for MN-Mal0, MN-Mal3, and MN-Mal5, respectively (Fig. 5d). With vibration (100 Hz, 4.5 m s^{-1}), the recovery rates were closely identical to those observed with the applicator alone: 62.12 ± 12.11 %, 66.47 ± 6.01 %, and 69.79 ± 8.75 % for MN-Mal0, MN-Mal3, and MN-Mal5, respectively (Fig. 5e).

The results demonstrated that ISF uptake can directly impact the recovery process where the difference was statistically significant ($p <$

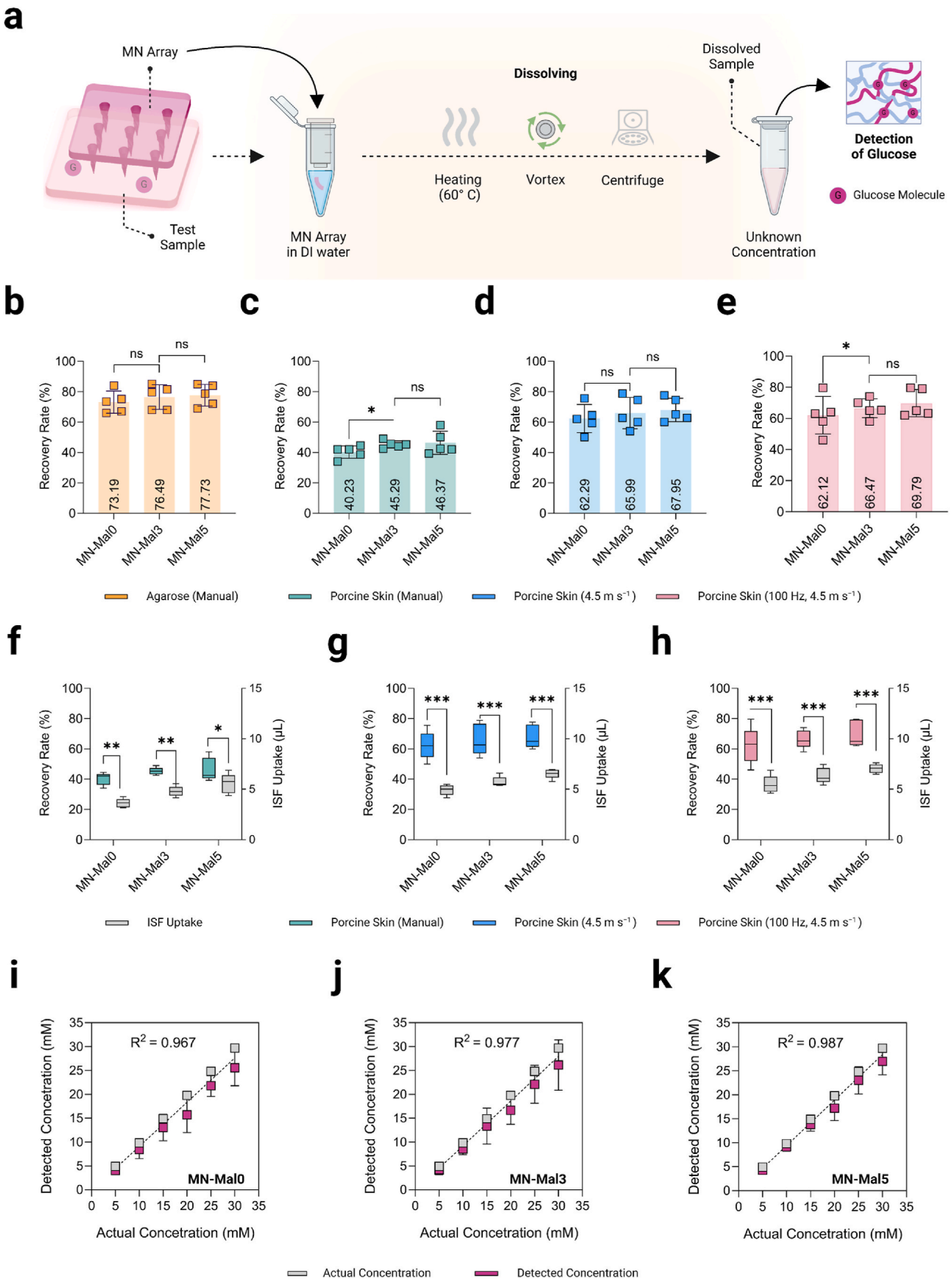

(caption on next page)

Fig. 5. Comprehensive assessment of the recovery of glucose across different techniques and models. a) Schematic illustration of the recovery process for glucose detection, showing the dissolution of the MNs in deionized (DI) water, followed by heating, vertexing, and centrifugation to release glucose molecules for subsequent analysis. b) Comparison of glucose recovery rates (%) from agarose gel using manual insertion for MN-Mal0, MN-Mal3, and MN-Mal5, indicating consistent recovery performance across all formulations. c) Recovery rates (%) of glucose from porcine skin using manual insertion, showing recovery efficiency for MN-Mal0, MN-Mal3, and MN-Mal5. d) Glucose recovery rates (%) from porcine skin with applicator-assisted insertion (0 Hz, 4.5 m s^{-1}), showing improved performance compared to manual insertion across all MN formulations. e) Glucose recovery rates (%) from porcine skin with vibration-assisted insertion (100 Hz, 4.5 m s^{-1}) for MN-Mal0, MN-Mal3, and MN-Mal5. f) Impact of ISF uptake (μL) from manual insertion on glucose recovery rates (%) for MN-Mal0, MN-Mal3, and MN-Mal5. g) Impact of ISF uptake (μL) from applicator-assisted insertion (0 Hz, 4.5 m s^{-1}) on glucose recovery rates (%) for MN-Mal0, MN-Mal3, and MN-Mal5. h) Impact of ISF uptake (μL) from vibration-assisted insertion (100 Hz, 4.5 m s^{-1}) on glucose recovery rates (%) for MN-Mal0, MN-Mal3, and MN-Mal5. i) Linear correlation between actual (grey) and detected glucose concentrations (purple) for MN-Mal0 ($R^2 = 0.967$) in agarose gel. j) Linear correlation between actual (grey) and detected glucose concentrations (purple) for MN-Mal3 ($R^2 = 0.977$) in agarose gel. k) Linear correlation between actual (grey) and detected glucose concentrations (purple) for MN-Mal5 ($R^2 = 0.987$) in agarose gel.

0.01, $p < 0.001$, $n = 5$). For example, the recovery rate increased proportionally with the volume of ISF extracted across all insertion methods (manual, 0 Hz, 4.5 m s^{-1}, and 100 Hz, 4.5 m s^{-1}) as well as different MN types (MN-Mal0, MN-Mal3, and MN-Mal5), (Fig. 5f–h). MN-Mal5 showed the highest ISF uptake; therefore, recovered glucose was higher than that of MN-Mal0 and MN-Mal3. The volume of ISF extracted is critical for accurate glucose concentration measurement, as lower ISF volumes may result in inadequate glucose concentrations, leading to inaccurate readings [31]. The same principle has been used in blood glucose testing, where a sufficient amount of blood is required in test strips to generate a measurable current for precise glucose quantification.

The findings also suggest a strong relationship between recovery rates and the critical metrics: ISF uptake, penetration depth, and penetration efficiency of the MNs, where higher ISF uptake consistently led to improved recovery rates. Additionally, greater penetration depth and efficiency further enhanced ISF uptake, directly impacting glucose recovery. The composition of the polymer matrix also plays a crucial role in determining the recovery rate, influencing the interaction between the MNs and tissue, as evidenced by varying recovery rates across different test models. Moreover, detected glucose concentrations (shown in purple) aligned closely with the actual concentration (shown in grey) across all MN types, with a strong correlation between measured and actual values (Fig. 5i–k).

2.5. Optimization of the SPE-based biosensor

For on-site glucose detection, SPEs were functionalized with PB, Chitosan-SWCNTs, GO_x- Bovine Serum Albumin (BSA), and Nafion (Fig. 6a) following an established protocol with slight modifications [32]. PB has been used as a mediator to enhance the sensitivity and selectivity of the sensor by reducing H_2O_2 [33,34]. Chitosan-SWCNTs improve enzyme immobilization and enhance electron transfer, while GO_x catalyzes glucose oxidation [35,36]. BSA helps stabilize the enzyme layer on the electrode, and Nafion acts as a permeability barrier, preventing interference from other analytes [37–39].

To activate the PB on the working electrode (WE), a CV test was performed in a 0.1 M KCl solution (scan rate 50 mV/s, 100 cycles), where it maintained consistent peak currents. Clear cathodic and anodic peaks were observed on the reversible transition between PB and Prussian white, indicating a robust redox process (Fig. 6b). As the scan rate increased from 10 to 50 mV/s, the peak currents increased linearly with the square root of the scan rate, further confirming a quasi-reversible redox mechanism (Fig. 6c). This linear relationship demonstrated the strong electrocatalytic activity of PB towards H_2O_2 reduction. Next, modified SPEs with GO_x were compared to those without GO_x (bare) at 5 mM glucose. The GO_x-modified electrodes showed a remarkably higher current response and clear redox peaks (Fig. 6d). In contrast, the bare SPE showed a minimal current response and lacked noticeable redox peaks.

Next, Nafion was applied to the modified SPEs to create a selective barrier where small molecules (e.g., glucose) could reach WE electrodes while filtering the other larger interfering molecules and preventing biofouling. To optimize the number of Nafion layers, two modified SPEs were compared: one with a single Nafion layer and the other with a double layer. CV test (50 mV/s) revealed that the SPE with a single Nafion layer responded to lower glucose concentrations, while the double-layered SPE required higher glucose levels for the same measurable response. Based on this observation, a single Nafion layer was selected for all subsequent analytical readouts.

To optimize the detection potential and calibrate the sensor, chronoamperometry was performed with 10 mM glucose in 0.1 M PBS across various potentials (– 0.00 V, – 0.05 V, – 0.10 V, – 0.15 V, and – 0.20 V). The background current in 0.1 M PBS was also recorded and compared to the glucose solution to identify the optimal balance between background noise and signal strength. The results showed that – 0.15 V had the highest average current with the lowest background interference, leading to the highest signal-to-background ratio (Fig. 6e and f). Therefore, – 0.15 V was chosen as the optimal potential for the final chronoamperometry tests. A range of glucose concentrations (0.5 mM–15 mM) was tested to confirm the biosensor's detection capability. Initially, 150 μL was applied to the electrode for each chronoamperometry test conducted at – 0.15 V over 60 s (Fig. 6g). The results demonstrated high sensitivity towards glucose, with the current directly proportional to the glucose concentration. The corresponding calibration curve demonstrated a strong linear relationship between current and glucose concentration ($R^2 = 0.980$) (Fig. 6h).

The sensor's current response was evaluated by progressively reducing the sample volume applied to the SPEs from 150 μL to 100 μL, 50 μL, 25 μL, and finally, 10 μL while maintaining a glucose concentration of 10 mM in a 0.1 M buffer solution. As shown in Fig. 6i-j, the current response remained stable for sample volumes ranging from 50 μL to 150 μL, indicating that these volumes provided adequate interaction between the sample and the electrode for accurate glucose detection. In contrast, noticeable changes in current response were observed when the sample volume was reduced to 25 μL and became even more pronounced at 10 μL. At these lower volumes, the sensor's ability to accurately detect glucose was potentially compromised, suggesting that the reduced contact area between the sample and the electrode may have impacted the sensor's performance. Therefore, 50 μL was identified as the minimum volume required for consistent and reliable glucose detection. The results further suggest a minimum incubation time of 9 min for the sensor to reach a steady-state current response. The high-density collagen matrix in the dermis acts as a barrier that restricts glucose movement and can lead to a longer equilibration time between blood plasma and ISF glucose levels. Since ISF lacks active circulation, glucose transport relies on passive diffusion, which is inherently slower in dense tissue environments. This results in a time lag between blood glucose fluctuations and their reflection in ISF.

The aISF/ISF with varying glucose concentrations (0.5 mM–15 mM) was extracted using the proposed MNs and dissolved to prepare samples for the SPE sensor. When the 50 μL of the sample was applied to the active site of the SPE, the 9-min stabilization period reflected the time required for glucose molecules to diffuse through the solution and reach the active site of the SPE (WE), where the electrochemical reaction generates a measurable current. This lag is consistent with the expected

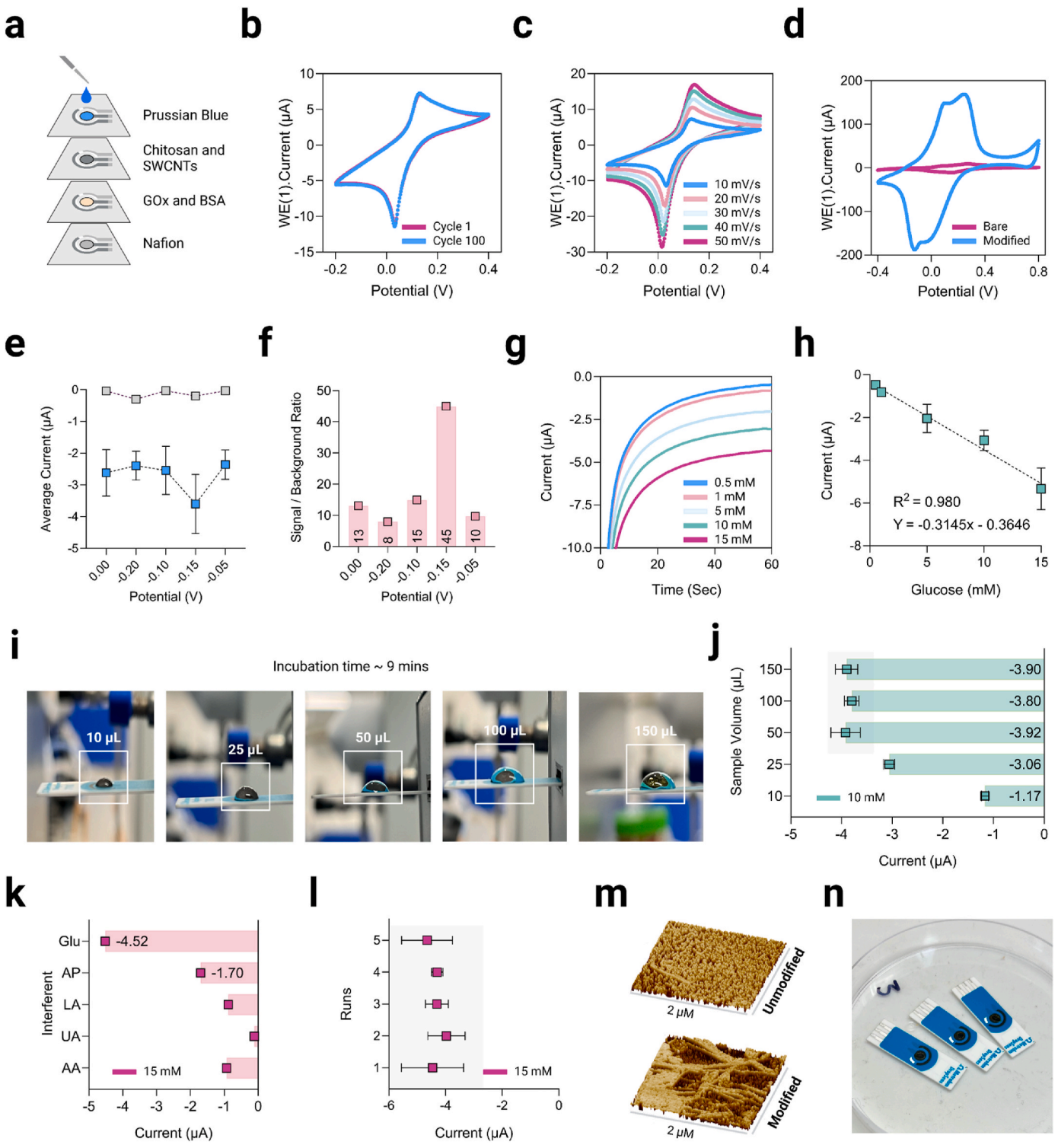

Fig. 6. Electrochemical characterization and optimization of the biosensor for glucose detection. a) Schematic illustration of the modification of the SPEs with Prussian blue, chitosan, SWCNTs, GO_x, BSA, and Nafion. b) CV of the sensor over 100 cycles showing stability of the Prussian blue. c) CV at different scan rates (10–50 mV/s) indicating scan rate-dependent response of the sensor. d) Comparison between the bare and modified SPEs demonstrating enhanced current response. e) Average current values at different applied potentials (0.00, – 0.05, – 0.10, – 0.15, – 0.20) in PBS (without glucose, grey) and with glucose (10 mM, blue). f) Corresponding signal-to-background ratio highlighting optimal potential range. g) Chronoamperometry response at varying glucose concentrations (0.5 mM–15 mM) indicating current response over time in 0.1 M PBS. h) Linear calibration plot of the sensor response for glucose detection (0.5 mM–15 mM), R^2 of 0.980 (n = 12). i) Images of the SPE at varying sample volumes (10–150 μL) with an incubation time of ≈9 min. j) Analysis of sample volume (μL) influence on current response for 10 mM glucose. k) Interference study showing current response to glucose (Glu), compared to AP, LA, UA, and AA at 15 mM glucose. l) Repeatability test of the sensor response over multiple runs at 15 mM glucose. m) AFM images of unmodified and modified WE showing surface morphology changes (2 μm × 2 μm). n) Image of the optimized SPEs for subsequent electrochemical analysis.

behavior of ISF-based glucose detection systems, as the diffusion of glucose in ISF is quicker than the sensor's response time, which includes the additional time needed for glucose to interact with the electrode surface. Therefore, a 9-min incubation time was maintained to ensure that the sample had sufficient time to fully interact with the surface of the WE before the test was run. This consistent time ensured that the sensor response was not influenced by differences in contact time, which could have introduced variability in the results.

The selectivity of the biosensor was assessed using common interferents found in ISF (e.g., acetaminophen (AP), lactic acid (LA), uric acid (UA), and ascorbic acid (AA). As shown in Fig. 6k, the glucose (Glu) response at 15 mM was significantly higher (– 4.52 μA) compared to the other interferents. Although AP showed some current response (– 1.70 μA), it was considerably lower, and LA, UA, and AA displayed negligible responses. This indicated that the sensor maintained high selectivity for glucose, even in the presence of these common interferents. Additionally, repeatability tests were conducted, as shown in Fig. 6l, where multiple runs (n = 5) were performed with 15 mM glucose, and the current response remained reasonably consistent. Fig. 6m shows the AFM images of both the modified and bare WE, revealing distinct morphological changes in surface properties. The bare WE exhibited a relatively smooth surface with lower surface roughness ($R_q = 23 \pm 4.51$ μm). In contrast, the modified WE exhibited a much more textured surface, with a significant increase in surface roughness ($R_q = 42 \pm 6.47$ μm). Fig. 6n shows the optimized SPEs prepared for glucose detection in ISF.

2.6. Direct detection of glucose using the optimized biosensor

The MN patches were evaluated with the electrochemical biosensor for direct glucose detection *in-vitro* without the need for any post-processing methods. After extracting aISF, MNs were dissolved to test the varying glucose concentrations (0.5 mM–15 mM) present within them. 50 μL of the prepared sample was applied on the WE, and chronoamperometry was performed for 60 s to record the partially amplified current using a potentiostat. Results suggest that the current response of the biosensor was linearly increased with the concentration of glucose. Fig. 7a and c shows the corresponding standard curve between glucose concentration (0.5 mM–15 mM) and the response of three MN samples showing a strong linear correlation, with MN-Mal5 demonstrating the highest linearity ($R^2 = 0.9971$). The slope of the standard curve was calculated as 1.217 μA/mM (MN-Mal0), 1.190 μA/mM (MN-Mal3) and 1.2 μA/mM (MN-Mal5), where the diameter of the WE was 4 mm. The LoD (3σ/S) of the biosensor for each MN type was almost identical and calculated as 0.07 mM (MN-Mal0), 0.08 mM (MN-Mal3) and 0.08 mM (MN-Mal5), where σ is the standard deviation (n = 5) of the background signal at the lowest concentration of glucose (0.5 mM) and S is the slope of each calibration curve (Fig. 7d). LoD is primarily influenced by factors such as the sensitivity of the electrode material, stability of the electrochemical reaction, and the background current in the measurement system. In this case, the near-identical LoDs suggest the consistency of the biosensor to reliably detect but not necessarily quantify the glucose concentration as low as 0.07 mM. The sensitivity of the biosensor was 9.68 μA mM^{-1} cm^{-2} (MN-Mal0), 9.46 μA mM^{-1} cm^{-2} (MN-Mal3) and 9.54 μA mM^{-1} cm^{-2} (MN-Mal5) (Fig. 7e). Additionally, MNs were

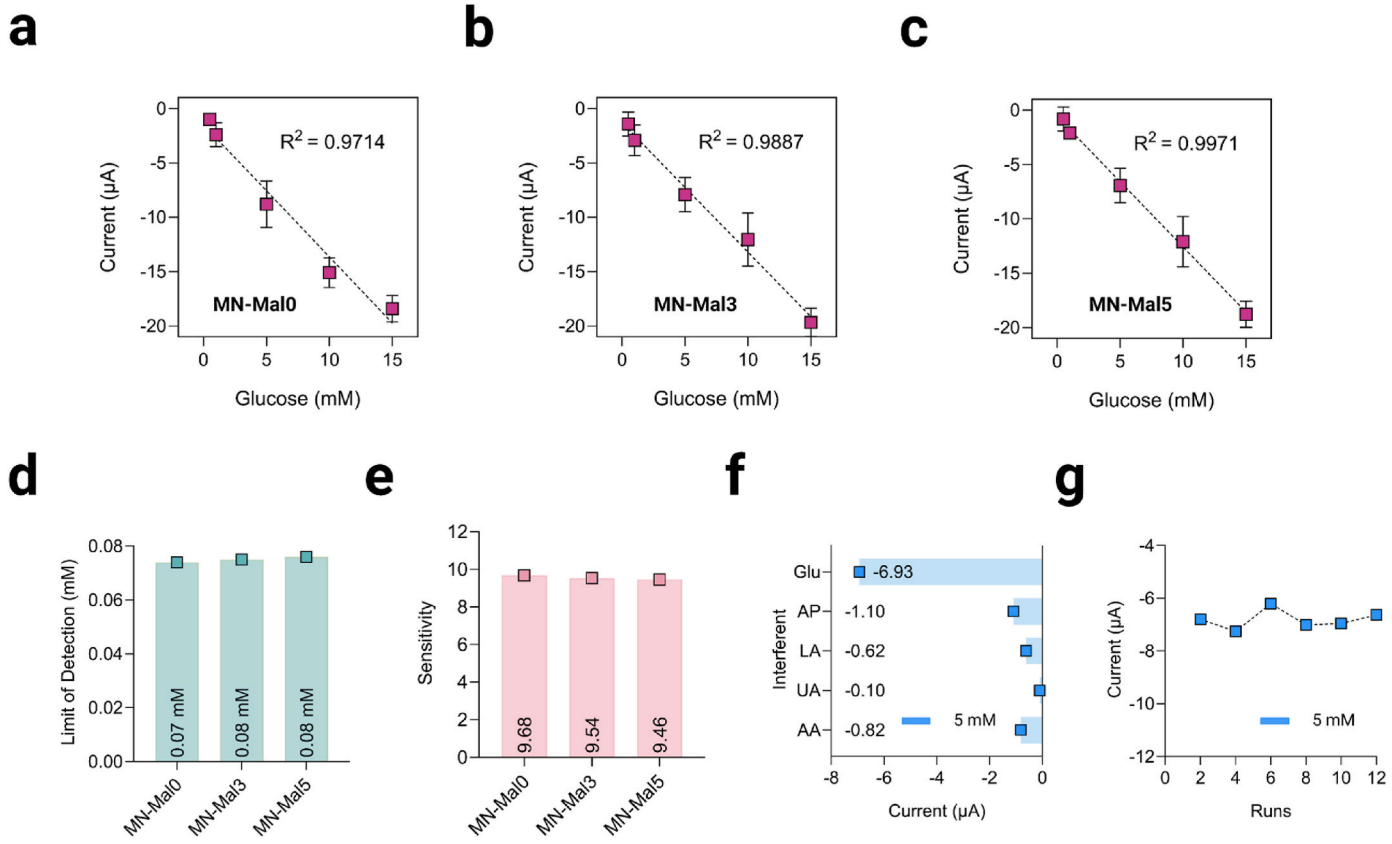

Fig. 7. MN-based biosensor system for direct glucose detection. a) MN-Mal0 indicating good correlation ($R^2 = 0.9714$) between glucose concentration (mM) and current (μA). b) MN-Mal3 showing good linearity ($R^2 = 0.9887$) between glucose concentration (mM) and current (μA). b) MN-Mal5 also indicates good linearity ($R^2 = 0.9971$) between glucose concentration (mM) and current (μA). d) The detection limit (mM) for glucose concentration across the three different MNs. e) The sensitivity (μA mM^{-1} cm^{-2}) of the biosensor remains consistent (9.46–9.68 μA mM^{-1} cm^{-2}) across all MN types. f) The sensor's selectivity towards other interferents such as AA, UA, LA, and AP. Glucose shows a sharp current response (– 6.93 μA), while other interferents show minimal current. g) Repeated measurements at 5 mM glucose concentration showing consistency with low variation in current response across different runs (n = 12).

further tested separately for the selectivity test on agarose gel containing aISF with common interferent (AP, LA, UA, AA) and with the presence of glucose (5 mM). The results highlight a significantly higher current in the presence of glucose compared to the current response from the interferents (Fig. 7f). It is evident that the sensor is highly selective towards glucose and expected to be not interfered with by other common substances present in ISF. In terms of sensor stability, the relative standard deviation (RSD) was calculated as 5.37 % based on multiple runs (Fig. 7g). The consistent current response across the repeated measurements indicates good sensor stability [40,41].

3. Challenges and considerations in translation of the technology

MN patches present promising opportunities as a practical alternative to conventional blood tests. This study presented a novel swellable MN patch and a biosensing platform to enable on-site glucose detection through an optimized applicator-assisted insertion method. Despite the advances and developments of MN technology so far, several challenges remain during the fabrication, administration, and commercialization process that need to be considered to make it a viable commercial product. Therefore, further research is required to develop a sound commercial product. Some of the key challenges and considerations are discussed in this section.

MN Manufacturing: MNs are manufactured using various techniques, each suitable for making specific materials. Manufacturing methods come in different fabrication times, accuracy, production costs, robustness, precision, and limitations. While the experimental techniques can effectively yield high-fidelity MNs for research or small-batch production, industrial-scale commercialization often requires automation and high-throughput processes. For example, 3D printing can be programmed sequentially to produce the MN patches in batch. At the same time, automation of the mold filling and demolding process can create opportunities for mass-scale production of MN patches [42]. Overall, advanced 3D printing platforms could enable faster production by directly printing MN patches from the formulated swellable material solution. Dimensional parameters, including the expected shrinkage during 3D printing, can be adjusted by optimizing print settings and design specifications. If mold replication (e.g., PDMS-based) is preferred, improving the mold-filling, drying and demolding steps can also significantly reduce the production time. Adapting the current methods with more scalable approaches would be essential before large-scale commercial development could be achieved.

MN Biocompatibility: Ensuring the biocompatibility of materials is fundamental to developing safe and effective MN patches. The materials used for the proposed patches are generally considered biocompatible. For example, the small amount (4 %, w/v) of PVA used in the MN solution is a biocompatible, water-soluble polymer commonly found in MN formulations [9,26,43–45]. Therefore, it is highly unlikely to accumulate in the skin or local draining lymph nodes during application. Instead, it may gradually break down into components the body naturally excretes (e.g., in urine). However, high concentrations of PVA may accumulate in lymph nodes and potentially lead to tissue reactions or organ effects [46], which is not the case in MN applications.

MN application time: For successful extraction and reliable biosensing, the developed MNs must remain inserted for 5 min, providing enough time to collect higher volume (>5 μL) of ISF. Although prolonged application times (>5 min) may offer higher ISF uptake, they can be impractical and increase discomfort. While blood tests using hypodermic needles can be conducted in a few minutes, the time required to visit a medical facility and have blood drawn by a trained professional is often more time-consuming and may not be an option in resource-limited settings. In contrast, MN patches have the potential to be self-administered, and biomarkers such as glucose can be detected with high accuracy within a short period. Application times of less than 5 min may reduce the extracted ISF volume, potentially nullifying the detection of glucose concentration in the ISF, as discussed earlier. Therefore, a 5-min application time was deemed reasonably acceptable for the MN patches to be effective in biosensing applications.

MN insertion method: The insertion technique is an equally important factor for ensuring reliable performance. As discussed earlier, the proposed applicator-assisted method is critical for achieving consistent and precise MN penetration. By controlling both the velocity and angle, the applicator presented in this study enabled reproducible and accurate insertion, minimizing variability and enhancing the performance of the overall insertion process in point-of-care. In contrast, without an applicator, insertion relies on manual application, which can vary from person to person, leading to inconsistent depth, uneven force, and potential discomfort or reduced effectiveness. The proposed applicator also provides a simple feedback system (a click) through the insertion trigger system to confirm the successful activation of the plunger on the test sample during insertion. Moreover, the applicator system relates to the principles of impact velocity and vibration mechanisms commonly used by mosquitoes and honeybees for enhanced insertion and efficiency [47,48]. During application, the applicator delivers a consistent impact at 4.5 m s^{-1} (with and without vibration) onto the sample, improving the overall performance of the MN application, which is discussed in this study and our previous work [49]. While the current experimental applicator system primarily assessed the feasibility of impact velocity (4.5 m s^{-1}) and vibration (100 Hz) on MN penetration, extraction, and recovery, future miniaturized versions could incorporate microelectronics for real-time feedback and suction capabilities that are similar to the existing commercial systems [50].

MN stability, storage and packaging: Proper storage is also important to ensure the stability of MN patches, as environmental factors such as temperature and humidity can significantly impact their mechanical strength. After peeling off the MN from the molds, the patches were stored at 4 °C for further use. The MN patches remained stable in standard room temperatures (25 °C–30 °C) under a controlled environment (e.g., incubator). Exposing the proposed MN patches to direct heat (e.g., sunlight) or leaving them at temperatures above 30 °C for extended periods (e.g., >24 h) can cause them to dissolve partially. To prevent damage during transportation, MN patches should be packaged with desiccants to control the moisture. Cold chain logistics (4 °C) can help maintain stability, and clear storage guidelines on the packaging can assist distributors and end users maintain the integrity of the MNs; however, this requires further and more detailed research optimization.

MN disposal: Since the MN patches are small and made of biocompatible materials, they can be safely disposed of in regular waste. However, swellable MNs are designed to be dissolved after extraction and be used on the SPEs for glucose detection. The leftover solution typically contains dissolved MN materials and a small volume of ISF. Under most circumstances, this solution can be disposed of down the drain or with regular laboratory liquid waste, provided it does not contain any hazardous substances. However, local regulations and institutional guidelines for biomedical or chemical waste disposal should always be followed to ensure safety and compliance.

Safety regulations and sterility: Regulatory considerations can also play a crucial role in ensuring the safe use of MNs. Breaking the skin barrier introduces potential infection risks; therefore, regulatory bodies such as the TGA (Therapeutic Goods Administration, Australia) or FDA (Food and Drug Administration, USA) require sterilization of the MN patches [51,52]. For example, gamma radiation sterilization can be used to sterilize the proposed MN patches and remove microorganisms without damaging the MN structure or functionality of the material.

An overall structured framework for the MN patch development and safety considerations is shown in Fig. 8.

4. Conclusion

The increasing demand for non-invasive, efficient methods for ISF extraction for biomarker analysis has highlighted the limitations of

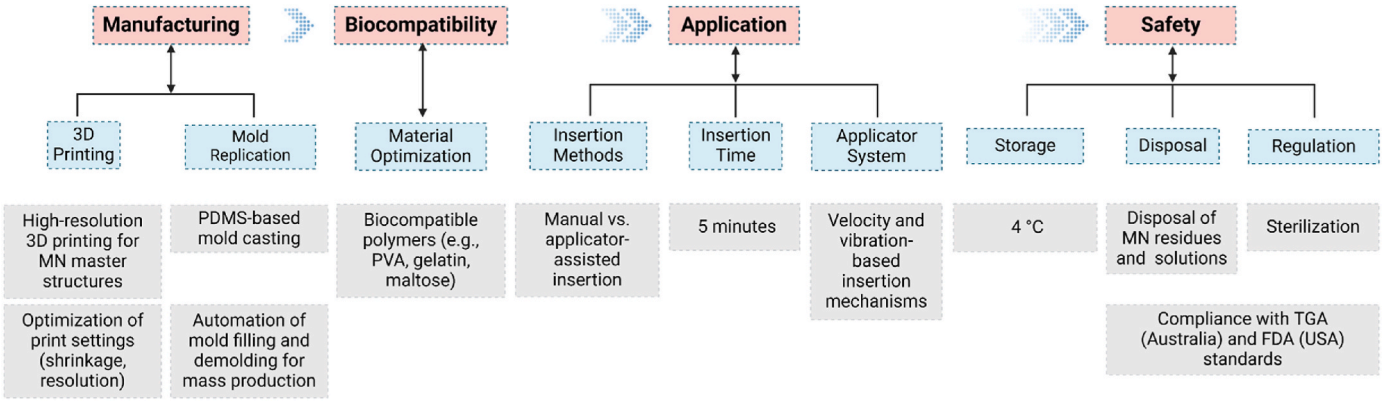

Fig. 8. A structured overview of the key aspects of MN patch development, application, and safety considerations. The framework comprises four main categories: manufacturing, biocompatibility, application, and safety.

traditional approaches, particularly in obtaining sufficient fluid volumes within an acceptable time. To address these challenges, this study successfully developed a novel osmolyte-driven spiral MN platform that can rapidly collect ISF and facilitate on-site glucose detection using an electrochemical biosensor. The MN design with interlocking capability, made from a swellable polymer matrix with gelatin, PVA, SAP, and osmolytes (maltose), effectively addressed these challenges by enabling rapid ISF extraction of ≈7 μL in just 5 min while maintaining the structural integrity during skin penetration.

Introducing an applicator-assisted insertion method greatly improved penetration ISF uptake, efficiency and depth compared to traditional manual insertions. This standardized approach reduced variability and user error, ensuring consistent ISF extraction across different applications. The ability to directly detect glucose from the recovered ISF using SPEs without post-processing offers a significant advantage over traditional blood glucose testing. The large volume extracted coupled with one-time SPEs should be sufficient for on-site glucose monitoring, with potential applications beyond diabetes management to detect other biomarkers in ISF. Thus, developing this MN-based biosensor system addresses the need for a highly efficient, minimally invasive, and user-friendly platform for glucose management in clinical and non-clinical settings, paving the way for broader diagnostic applications and personalized healthcare solutions.

5. Experimental section

5.1. Materials and instrumentations

Polyvinyl alcohol (PVA, Mw 89 kDa, fully hydrolyzed), gelatin from porcine skin (type A, 300g bloom), D-glucose, agarose (low EEO), Dulbecco's phosphate-buffered saline (PBS, pH 7.1–7.5), bovine Serum Albumin (BSA, purity ≥96 %), glucose oxidase from Aspergillus niger (type X–S), ascorbic acid (AA), sodium L-lactate (purity ≥99 %), lactic acid (LA), uric Acid (UA), acetaminophen (AP), Poly (acrylic acid, sodium salt, Mw ~8,000, 45 wt% in H_2O, SAP), solutionPrussian blue, Rhodamine B (purity ≥95 %), single-walled carbon nanotube (purity ≥98 %) and Parafilm® were purchased from Sigma-Aldrich (St. Louis, MO, USA).

Sylgard 184 silicone elastomer was obtained from Dow Corning (Midland, MI, USA). Artificial interstitial fluid (aISF, pH 7.4) was purchased from Biochemazone (Alberta, Canada). A commercial glucometer (Accu-Chek, Roche Diagnostics, IN, USA) was purchased from Chemist Warehouse (Brisbane, Queensland, Australia). Nafion™ D520CS (alcohol based 1000 EW at 5 % weight) was purchased from Ion Power Inc. (Detroit, USA). Screen-printed electrodes (SPE) and connectors for SPEs (DSC4MM) were obtained from Metrohm (Gladesville, NSW, Australia). Autolab potentiostat (PGSTAT302 N, Metrohm) with NOVA (version 2.1) was used for electrochemical characterization.

Freshly butchered (<36 h) porcine skin was obtained from a local butcher shop (Queensland, Australia). Experiments were conducted under the approval of the Ethics Committee of the University of Southern Queensland (UniSQ), Australia (Ethics approval number: 23BIOS008). All materials used in this study were of the highest quality and were used without further purification.

5.2. Master MN patch and PDMS negative mold preparation

Master MNs were designed in SolidWorks 2024 (Dassault Systèmes, SolidWorks Corporation, MA, USA) with a 1 mm height and 0.3 mm base diameter. The design incorporated two squares within the structure to produce the anti-clockwise twist. The master patch was fabricated using the state-of-the-art microArch® S240 3D printer (BMF, Maynard, MA, USA) using silicone castable resin. Post-printing, MNs were cleaned with ethanol to remove any uncured resins and washed in ultra-pure water. The master MN patches were used to create the negative molds using soft lithography. To prepare the PDMS solution, the silicone elastomer base and curing agent (SYLGARD 184 Silicone Elastomer Kit, Dow Corning, Midland, MI, USA) were mixed at a 10:1 ratio (base: agent) and centrifuged (Kurabo KK-50S, Kurabo Electronics, OSK, Japan) for 4 min. The mixture was poured onto the master MN patch placed in the center of a Petri dish and cured at 90 °C for 2 h in a laboratory oven (Labwit Scientific, ZXRD-A5055, Australia). Once fully cured, the PDMS was peeled off from the mold for MN replication.

5.3. Fabrication of the swellable MNs

A 6 % (w/v) gelatin was added to warm ultrapure water and stirred vigorously at 70 °C until completely dissolved. A 4 % (w/v) PVA solution was prepared separately in PBS while continuously stirring at 70 °C overnight to ensure proper mixing. A small amount of SAP was added to the homogenous PVA solution, which was then stirred and sonicated for an additional 6 h at 70 °C. The gelatin and PVA (6/4, w/v) mixture was then vortexed and sonicated to prepare the initial Gelatin/PVA solution. Afterwards, the temperature was reduced to 60 °C, and varying concentrations of maltose (0 %, 3 %, 5 %, w/v) were added to the mixture. The solution was stirred for another 4 h to incorporate the maltose fully. Finally, ≈180 μL of the prepared solution was added to the PDMS mold and centrifuged at 4000 rpm for 5 min, followed by four consecutive overfills at ≈ 45-min intervals. The MNs were then dried at room temperature for ≈36 h before being peeled off.

5.4. Morphology characterization of MNs

The morphology of the spiral MNs was analyzed using a digital

microscope (DSX1000, Olympus, Japan) at varying magnifications (× 20 and × 40). The imaging process included adjustable tilt angles between 0° and 45° to capture detailed views of the structures. The captured images were post-processed using the LEXT (Olympus, Japan) software. The spiral MNs were further examined using a scanning electron microscope (SEM, JSM-7001F, JEOL, Japan) for a more detailed assessment. To prevent charging during SEM imaging, the MNs were sputter-coated with a 12 nm layer of platinum. The SEM images were captured in high vacuum mode (HighVac) at an accelerating voltage of 10 kV and a magnification of × 50. The MN patches were carefully de-molded immediately before imaging to avoid damage.

5.5. Swelling tests in aISF

To determine the swelling ratio of MNs, the initial dry weight of the MN patch (W_d) was recorded and then submerged in aISF at 37 °C for 5 min to record the wet weight (W_w) at 1-min intervals. Since the application time for MNs should be short (>5 min), weight changes over only 5 min were considered and calculated using the following formula:

$$\text{Swelling ratio } (\%) = \left[\frac{W_w - W_d}{W_d} \right] \times 100 \quad (1)$$

5.6. Mechanical compression test

Compression tests were performed to evaluate the mechanical properties of the MN patches. A 15 × 15 MN patch was attached to the fixed plate of a low-force UTM (Instron 3343, Instron, MA, USA) using double-sided tape to secure the needle-side up. The MN patch was subjected to compression at a speed of 0.5 mm/min, reaching a maximum displacement of 0.5 mm under a 50 N static load cell. Throughout the test, force-displacement data was collected to calculate the compressive modulus (E) from the stress (σ) and strain (ϵ) curves.

$$\text{Stress } (\sigma) = \frac{F}{A} \quad (2)$$

$$\text{Strain } (\epsilon) = V(t\text{-}t_0) \quad (3)$$

$$\text{Compressive modulus } (E) = \frac{\sigma}{\epsilon} \quad (4)$$

Where F is the applied compressive force (N), A is the cross-sectional area of the MN patch where the compressive force is applied (mm^2), V is the set rate of the load cell of the UTM, t is time of elastic deformation and t_0 is an approximate time when the load cell first reaches the MNs.

5.7. Setup of MN applicator system

The custom-designed MN applicator was fabricated using a 3D printer with polylactic acid (PLA) filament based on the dimensions from our previous studies [22]. The setup included Eccentric Rotating Mass (ERM) vibration motors, a diode rectifier, a lithium polymer battery, a potentiometer, transistors, and resistors, all managed through the Arduino Integrated Development Environment (IDE). This configuration allowed for real-time adjustments to vibration frequencies, which could be adjusted through the IDE programming. In the modified version of the applicator, two ERM motors were positioned parallel to the plunger to generate symmetrical, transverse vibrations. This dual-motor arrangement, controlled by Arduino IDE, improved the uniformity of vibration across the plunger head, which addressed the limitation of earlier designs that used a single motor that may produce non-uniform vibrations. The Arduino platform enabled precise control of vibration frequency (100 Hz) through the Arduino IDE, eliminating the inconsistencies associated with the potentiometer knob. However, the potentiometer was retained as a backup for manual voltage adjustment to the motors, ensuring flexibility in the absence of the Arduino IDE. The added transistors were to amplify the signal, whereas diodes were to protect against reverse voltage spikes. Additionally, resistors were used to regulate the current flowing through the transistors and motors for safe and efficient functionality. The plunger's speed was set at 4.5 m s^{-1}, generating an impact energy of 215.46 mJ. The applicator was activated via a push-button mechanism to strike the test sample. The impact velocity was validated through high-speed camera analysis and theoretical modeling, as established in our earlier studies [21]. Fig. 9a and b illustrates the circuit configuration and shows the design configuration of the applicator system, including key components, connections, and an image view of the circuit assembly.

5.8. Extraction, detection and recovery of ISF In vitro and ex-vivo

A 1.4 % (w/v) agarose gel was prepared in aISF containing different glucose (5 mM–30 mM). MN patches were applied to the agarose model for 5 min to simulate ISF extraction. The change in weight before (W_d) and after insertion (W_w) was measured using the following formula to determine the volume of ISF extracted:

$$\text{ISF Volume Extracted } (\mu L) = W_w - W_d \quad (5)$$

For the *ex-vivo* model, fresh porcine skin was sourced from a local butcher, then cut into small blocks (3 cm × 3 cm) and soaked in aISF for 30 min. The thickness of the porcine skin was measured at ≈ 3 mm. Any excess aISF was wiped off, and the skin was placed on an anti-slip surface. The holes were inspected, and depth was captured using a digital microscope (DSX 1000, Olympus, Japan) and assessed using the advanced function of the LEXT software (Olympus, Japan). After removal, the MN patch was immediately transferred to a tube containing 50 μL of PBS solution and heated at 60 °C for 15 min to dissolve. The sample was then vortexed for 1 min to ensure complete dissolution, followed by centrifugation at 4000 rpm for 5 min to prepare the sample solution. The sample supernatant was collected and analyzed using a highly sensitive glucometer for glucose concentration, and the recovery percentage of glucose was calculated using the following formula:

$$\textit{Glucose Recovery } (\%) = \frac{\textit{Detected glucose concentration } (\text{mM})}{\textit{Actual glucose concentration } (\text{mM})} \times 100 \quad (6)$$

5.9. Insertion efficiency and penetration depth of MNs

A commercially available Parafilm sheet was folded into eight layers (each 127 μm thick, totalling ≈ 1 mm) to mimic human skin for the initial insertion test. The MN patch was then applied to this setup, using both manual insertion and with the custom applicator without vibration (0 Hz, 4.5 m s^{-1}) and with vibration (100 Hz, 4.5 m s^{-1}). After applying the MN patches, each layer of the Parafilm model was examined for successful penetration. The micro-holes were counted across the layers to assess the number of successful insertions. Insertion efficiency was calculated using the following formula:

$$\textit{Insertion Efficiency } (\%) = \frac{\textit{Number of MN successfully penetrated}}{\textit{Total number of MNs}} \times 100 \quad (7)$$

To measure penetration depth, high-resolution images of the micro-holes were captured using the DSX 1000 microscope and LEXT software. The penetration depth was determined by counting the number of Parafilm layers pierced and further validated using LEXT software analysis using the following formula:

$$\textit{Total Penetration Depth} = L_1 + L_2 + L_3 + \cdots + L_n \quad (8)$$

Where each L represents the thickness of a pierced layer.

Similarly, insertion efficiency and penetration depth were assessed on porcine skin using the DSX 1000 microscope, following the preparation method described previously. The application sites on the skin

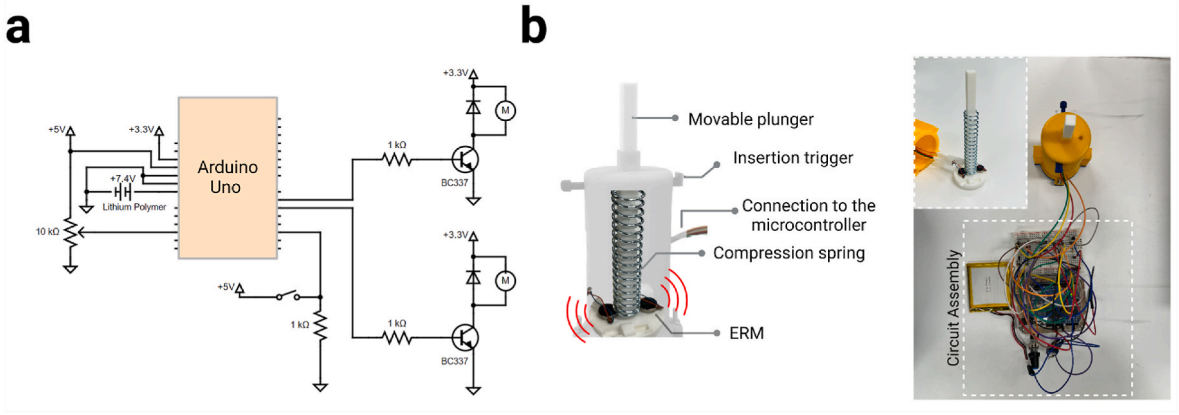

Fig. 9. Schematic of the circuit and design of the applicator system for MN insertion. a) Circuit diagram illustrating the Arduino Uno microcontroller connection to other electronic components of the system. b) Internal configuration of the applicator, featuring a movable plunger, insertion trigger, compression spring, and connection to ERM motors for vibration, along with a circuit assembly to power and control the system.

were examined for micro-holes, and insertion efficiency was calculated in the same way as for Parafilm. For penetration depth, the microscope's advanced digital features were used to create a 3D image of the insertion hole and quantified by converting the 3D image data into numerical values.

For the agarose gel model (1.4 % w/v), the primary focus was ISF extraction. However, for consistency, penetration holes and depth were analyzed using the same methodology as Parafilm and porcine skin for a uniform approach across all models.

5.10. Screen-printed Prussian blue/carbon electrode

The experiments used commercially available screen-printed electrodes (SPEs) from Metrohm DropSens (Gladesville, NSW, Australia) printed on a 34 mm × 10 mm × 0.05 mm ceramic substrate. The setup included a conventional three-electrode system: a working electrode (WE), a counter electrode (CE), and a reference electrode (RE). WE was modified using Prussian blue/carbon, CE was made from carbon, and the RE was made of silver (A_g).

5.11. Preparation for the glucose detection

First, the impact of SWCNTs on the amperometric responses of bare and MWCNT-modified electrodes was evaluated (Fig. S4). Then, an enzymatic layer containing GO_x, BSA, and chitosan modified with SWCNTs was applied to the SPE for selective glucose detection. Briefly, 1 wt% chitosan solution was prepared in 50 mM acetic acid under mild heat (50 °C) with continuous stirring overnight. SWCNTs were added to the chitosan solution and mixed for 1 h. Next, 3 μL of the chitosan-SWCNT mixture was applied to the WE and allowed to dry for 30 min. Following this, 3 μL of a 50 mg/mL GO_x solution with a 15 mg/mL BSA solution were drop-cast onto the working electrode and dried overnight at – 4 °C. GO_x and BSA stock solutions were stored in the freezer at – 20 °C while the chitosan mixture was stored at – 4 °C. To help prevent interference from negatively charged substances that can affect accurate glucose detection, 2 μL of a 0.5 wt% Nafion solution was applied to the WE as a selective barrier and allowed to dry for 30 min. The biosensor was then stored at – 4 °C before the electrochemical analysis.

5.12. Immobilization of GOx and Chronoamperometric measurement

In order to assess the effect of GO_x, two separate electrodes were investigated in the presence and absence of GO_x (bare) within the buffer solution (0.1 M PBS) with varying glucose concentrations (0 mM–15 mM). GO_x binds in the presence of glucose and facilitates oxidation by producing hydrogen peroxide (H_2O_2). The formed H_2O_2 oxidizes PB to change its reduced state (PB_{red}) to an oxidized state (PB_{ox}). The produced PB is then reduced back to PB_{red} on the WE at an applied voltage. During the process, PB acts as a catalyst mediator in the reduction of H_2O_2 that allows low potential selective detection of H_2O_2 at a potential that is nearly 0 V. This low potential is necessary to prevent the oxidation of interfering substances. The current produced during the reduction of PB_{ox} reacts with electrodes and is proportional to the concentration of glucose. Equations (9) and (10) shows the working mechanism of glucose detection using the Prussian blue/carbon electrode:

$$\text{Glucose} + O_2 \xrightarrow{GOx} \text{Gluconic Acid} + H_2O_2 \quad (9)$$

$$H_2O_2 \xrightarrow{PB} O_2 + 2H^+ + 2e^- \quad (10)$$

The amperometric response of the biosensor was measured in 0.1 M PBS solutions with the same glucose concentrations varying from 0 mM to 15 mM based on typical glucose levels in human ISF. A low potential of – 0.15 mV was applied between RE and WE and ran for 60 s to generate the current produced by the reduction of H_2O_2. Starting at a 0 mM glucose concentration, the concentration was increased to 15 mM separately to prepare and mix the solution after the addition of glucose.

5.13. Calibration and detection limits of biosensor

The obtained average current value (with glucose) was adjusted by subtracting the average background current (without glucose). These net current values at each glucose concentration were then plotted against the corresponding known glucose concentrations to generate a calibration curve. The limit of detection (LoD) was calculated using the formulas below:

$$\text{Limit of detection (LoD)} = \frac{3\sigma}{S} \quad (11)$$

Where σ is the standard deviation of the background signal response, and S is the slope of the calibration curve.

5.14. Statistical analysis

All experiments were performed five times (n = 5), and data were presented as mean ± standard deviation (SD). Statistical analyses were performed in GraphPad Prism (version 10.0), where group differences were analyzed using a two-tailed *t*-test for pairwise comparisons, and one-way ANOVA with Tukey's post-hoc test was employed for multiple group comparisons. P-values <0.05 were considered statistically significant, with significance levels denoted as *p < 0.05, **p < 0.01, ***p

< 0.001, and ns = non-significant differences.

CRediT authorship contribution statement

Khaled Mohammed Saifullah: Writing – review & editing, Writing – original draft, Visualization, Validation, Software, Methodology, Investigation, Formal analysis, Data curation, Conceptualization. **Pouria Azarikhah:** Writing – review & editing, Visualization, Software, Methodology, Conceptualization. **Zahra Faraji Rad:** Writing – review & editing, Validation, Supervision, Software, Resources, Project administration, Methodology, Investigation, Formal analysis, Conceptualization.

Declaration of competing interest

The authors declare the following financial interests/personal relationships which may be considered as potential competing interests: Zahra Faraji Rad has patent #PCT/AU2023/050626 issued to University of Southern Queensland. If there are other authors, they declare that they have no known competing financial interests or personal relationships that could have appeared to influence the work reported in this paper.

Acknowledgements

This work used the Queensland node of the NCRIS-enabled Australian National Fabrication Facility (ANFF). The study undertaken would not have been possible without the generous support of AXT Pty Ltd. Specific acknowledgement goes to Jaret Lee and Bradman Marks from AXT for their assistance in microfabrication using a state-of-the-art projection micro stereolithography (PμSL) system from Boston Micro Fabrication. Special thanks to Dr Asim Mushtaq from UniSQ for his suggestions during the solution preparations. The author would also like to acknowledge Dr Choman Salih from UniSQ for his assistance in facilitating access to multiple laboratories. This research received no specific grant from any funding agency in the public, commercial, or not-for-profit sectors.

Appendix A. Supplementary data

Supplementary data to this article can be found online at https://doi.org/10.1016/j.mtchem.2025.102661.

Data availability

Data will be made available on request.

References

[1] A.C. Müller, F.P. Breitwieser, H. Fischer, C. Schuster, O. Brandt, J. Colinge, G. Superti-Furga, G. Stingl, A. Elbe-Bürger, K.L. Bennett, A comparative proteomic study of human skin suction blister fluid from healthy individuals using immunodepletion and iTRAQ labeling, J. Proteome Res. 11 (2012) 3715–3727, https://doi.org/10.1021/PR3002035.

[2] J. Kool, L. Reubsaet, F. Wesseldijk, R.T. Maravilha, M.W. Pinkse, C.S. D'Santos, J. J. Van Hilten, F.J. Zijlstra, A.J.R. Heck, Suction blister fluid as potential body fluid for biomarker proteins, Proteomics 7 (2007) 3638–3650, https://doi.org/10.1002/PMIC.200600938.

[3] A. Tobias, B.D. Ballard, S.S. Mohiuddin, Physiology, water balance, StatPearls (2022). https://www.ncbi.nlm.nih.gov/books/NBK541059/. (Accessed 8 October 2024).

[4] P.R. Miller, R.M. Taylor, B.Q. Tran, G. Boyd, T. Glaros, V.H. Chavez, R. Krishnakumar, A. Sinha, K. Poorey, K.P. Williams, S.S. Branda, J.T. Baca, R. Polsky, Extraction and biomolecular analysis of dermal interstitial fluid collected with hollow microneedles, Commun. Biol. 1 (1 1) (2018) 1–11, https://doi.org/10.1038/s42003-018-0170-z.

[5] B.Q. Tran, P.R. Miller, R.M. Taylor, G. Boyd, P.M. Mach, C.N. Rosenzweig, J. T. Baca, R. Polsky, T. Glaros, Proteomic characterization of dermal interstitial fluid extracted using a novel microneedle-assisted technique, J. Proteome Res. 17 (2018) 479–485, https://doi.org/10.1021/ACS.JPROTEOME.7B00642.

[6] P. Bollella, S. Sharma, A.E.G. Cass, R. Antiochia, Microneedle-based biosensor for minimally-invasive lactate detection, Biosens. Bioelectron. 123 (2019) 152–159, https://doi.org/10.1016/J.BIOS.2018.08.010.

[7] M. Friedel, I.A.P. Thompson, G. Kasting, R. Polsky, D. Cunningham, H.T. Soh, J. Heikenfeld, Opportunities and challenges in the diagnostic utility of dermal interstitial fluid, Nat. Biomed. Eng. 7 (12 7) (2023) 1541–1555, https://doi.org/10.1038/s41551-022-00998-9.

[8] J. Zhu, X. Zhou, H.J. Kim, M. Qu, X. Jiang, K.J. Lee, L. Ren, Q. Wu, C. Wang, X. Zhu, P. Tebon, S. Zhang, J. Lee, N. Ashammakhi, S. Ahadian, M.R. Dokmeci, Z. Gu, W. Sun, A. Khademhosseini, Gelatin methacryloyl microneedle patches for minimally invasive extraction of skin interstitial fluid, Small 16 (2020) 1905910, https://doi.org/10.1002/SMLL.201905910.

[9] Y. Shi, D. Xiong, Y. Liu, N. Wang, X. Zhao, Swelling, mechanical and friction properties of PVA/PVP hydrogels after swelling in osmotic pressure solution, Mater. Sci. Eng. C 65 (2016) 172–180, https://doi.org/10.1016/J.MSEC.2016.04.042.

[10] R. He, Y. Niu, Z. Li, A. Li, H. Yang, F. Xu, F. Li, A hydrogel microneedle patch for point-of-care testing based on skin interstitial fluid, Adv. Healthcare Mater. 9 (2020) 1901201, https://doi.org/10.1002/ADHM.201901201.

[11] Y. Qiao, J. Du, R. Ge, H. Lu, C. Wu, J. Li, S. Yang, S. Zada, H. Dong, X. Zhang, A sample and detection microneedle patch for psoriasis MicroRNA biomarker analysis in interstitial fluid, Anal. Chem. (2022), https://doi.org/10.1021/ACS.ANALCHEM.1C04401 acs.analchem.1c04401.

[12] M. Zheng, Z. Wang, H. Chang, L. Wang, S.W.T. Chew, D.C.S. Lio, M. Cui, L. Liu, B. C.K. Tee, C. Xu, Osmosis-powered hydrogel microneedles for microliters of skin interstitial fluid extraction within minutes, Adv. Healthcare Mater. 9 (2020) 1901683, https://doi.org/10.1002/ADHM.201901683.

[13] E. Laszlo, G. De Crescenzo, A. Nieto-Argüello, X. Banquy, D. Brambilla, Superswelling microneedle arrays for dermal interstitial fluid (Prote)Omics, Adv. Funct. Mater. 31 (2021) 2106061, https://doi.org/10.1002/ADFM.202106061.

[14] H. Chang, M. Zheng, X. Yu, A. Than, R.Z. Seeni, R. Kang, J. Tian, D.P. Khanh, L. Liu, P. Chen, C. Xu, A swellable microneedle patch to rapidly extract skin interstitial fluid for timely metabolic analysis, Adv. Mater. 29 (2017), https://doi.org/10.1002/ADMA.201702243.

[15] P.P. Samant, M.R. Prausnitz, Mechanisms of sampling interstitial fluid from skin using a microneedle patch, Proc. Natl. Acad. Sci. U. S. A. 115 (2018) 4583–4588, https://doi.org/10.1073/PNAS.1716772115/SUPPL_FILE/PNAS.1716772115.SAPP.PDF.

[16] T. Abbasiasl, F. Mirlou, H. Mirzajani, M.J. Bathaei, E. Istif, N. Shomalizadeh, R. E. Cebecioğlu, E.E. Özkahraman, U.C. Yener, L. Beker, A wearable touch-activated device integrated with hollow microneedles for continuous sampling and sensing of dermal interstitial fluid, Adv. Mater. 36 (2024) 2304704, https://doi.org/10.1002/ADMA.202304704.

[17] P.P. Samant, M.M. Niedzwiecki, N. Raviele, V. Tran, J. Mena-Lapaix, D.I. Walker, E.I. Felner, D.P. Jones, G.W. Miller, M.R. Prausnitz, Sampling interstitial fluid from human skin using a microneedle patch, Sci. Transl. Med. 12 (2020), https://doi.org/10.1126/SCITRANSLMED.AAW0285/SUPPL_FILE/AAW0285_SM.PDF.

[18] X. Jiang, E.C. Wilkirson, A.O. Bailey, W.K. Russell, P.B. Lillehoj, Microneedle-based sampling of dermal interstitial fluid using a vacuum-assisted skin patch, Cell Rep. Phys. Sci. 5 (2024) 101975, https://doi.org/10.1016/j.xcrp.2024.101975.

[19] K. Takeuchi, N. Takama, B. Kim, K. Sharma, O. Paul, P. Ruther, Microfluidic chip to interface porous microneedles for ISF collection, Biomed. Microdevices 21 (2019) 1–10, https://doi.org/10.1007/S10544-019-0370-4/FIGURES/11.

[20] J. Chen, M. Wang, Y. Ye, Z. Yang, Z. Ruan, N. Jin, Fabrication of sponge-forming microneedle patch for rapidly sampling interstitial fluid for analysis, Biomed. Microdevices 21 (2019), https://doi.org/10.1007/S10544-019-0413-X.

[21] V. Ebrahiminejad, A. Malek-khatabi, Z. Faraji Rad, Influence of low-frequency vibration and skin strain on insertion mechanics and drug diffusion of PVA/PVP dissolving microneedles, Adv. Mater. Technol. 9 (2024) 2301272, https://doi.org/10.1002/ADMT.202301272.

[22] V. Ebrahiminejad, Z.F. Rad, P.D. Prewett, G.J. Davies, Fabrication and testing of polymer microneedles for transdermal drug delivery, Beilstein J. Nanotechnol. 13 (55 13) (2022) 629–640, https://doi.org/10.3762/BJNANO.13.55.

[23] P. Makvandi, M. Kirkby, A.R.J. Hutton, M. Shabani, C.K.Y. Yiu, Z. Baghbantaraghdari, R. Jamaledin, M. Carlotti, B. Mazzolai, V. Mattoli, R. F. Donnelly, Engineering microneedle patches for improved penetration: analysis, skin models and factors affecting needle insertion, Nano-Micro Letters 13 (1 13) (2021) 1–41, https://doi.org/10.1007/S40820-021-00611-9.

[24] O. Olatunji, D.B. Das, M.J. Garland, L. Belaid, R.F. Donnelly, Influence of array interspacing on the force required for successful microneedle skin penetration: theoretical and practical approaches, J. Pharmaceut. Sci. 102 (2013) 1209–1221, https://doi.org/10.1002/JPS.23439.

[25] A.M. Römgens, D.L. Bader, J.A. Bouwstra, F.P.T. Baaijens, C.W.J. Oomens, Monitoring the penetration process of single microneedles with varying tip diameters, J. Mech. Behav. Biomed. Mater. 40 (2014) 397–405, https://doi.org/10.1016/J.JMBBM.2014.09.015.

[26] N. Xu, M. Zhang, W. Xu, G. Ling, J. Yu, P. Zhang, Swellable PVA/PVP hydrogel microneedle patches for the extraction of interstitial skin fluid toward minimally invasive monitoring of blood glucose level, Analyst 147 (2022) 1478–1491, https://doi.org/10.1039/D1AN02288A.

[27] D.F.S. Fonseca, P.C. Costa, I.F. Almeida, P. Dias-Pereira, I. Correia-Sá, V. Bastos, H. Oliveira, C. Vilela, A.J.D. Silvestre, C.S.R. Freire, Swellable gelatin methacryloyl microneedles for extraction of interstitial skin fluid toward minimally invasive monitoring of urea, Macromol. Biosci. 20 (2020) 2000195, https://doi.org/10.1002/MABI.202000195.

[28] A.P. Nesterova, E.A. Klimov, M. Zharkova, S. Sozin, V. Sobolev, N.V. Ivanikova, M. Shkrob, A. Yuryev, Diseases of the skin and subcutaneous tissue, Disease Pathways (2020) 493–532, https://doi.org/10.1016/B978-0-12-817086-1.00011-7.
[29] M.B. Murphrey, J.H. Miao, P.M. Zito, Histology, stratum corneum, StatPearls (2022). https://www.ncbi.nlm.nih.gov/books/NBK513299/. (Accessed 28 October 2024).
[30] E. Larrañeta, J. Moore, E.M. Vicente-Pérez, P. González-Vázquez, R. Lutton, A. D. Woolfson, R.F. Donnelly, A proposed model membrane and test method for microneedle insertion studies, Int. J. Pharm. 472 (2014) 65–73, https://doi.org/10.1016/J.IJPHARM.2014.05.042.
[31] D. Li, R. Wang, H. Yu, G. Li, Y. Sun, W. Liang, K. Xu, A method for measuring the volume of transdermally extracted interstitial fluid by a three-electrode skin resistance sensor, Sensors 14 (2014) 7084–7095, https://doi.org/10.3390/S140407084, 14 (2014) 7084–7095.
[32] F. Davis, S.P.J. Higson, Glucose biosensors-recent advances in the field of diabetes management, Micro Fuel Cells: Principles Appl. (2009) 243–292, https://doi.org/10.1016/B978-0-12-374713-6.00006-8.
[33] L. Fernández, J. Alvarez-Paguay, G. González, R. Uribe, D. Bolaños-Mendez, J. L. Piñeiros, L. Celi, P.J. Espinoza-Montero, Electrochemical sensor for hydrogen peroxide based on prussian blue electrochemically deposited at the TiO2-ZrO2–doped carbon nanotube glassy carbon-modified electrode, Front. Chem. 10 (2022) 884050, https://doi.org/10.3389/FCHEM.2022.884050.
[34] M.P. O'Halloran, M. Pravda, G.G. Guilbault, Prussian Blue bulk modified screen-printed electrodes for H2O2 detection and for biosensors, Talanta 55 (2001) 605–611, https://doi.org/10.1016/S0039-9140(01)00469-6.
[35] J.S. Ye, Y. Wen, W. De Zhang, L.M. Gan, G.Q. Xu, F.S. Sheu, Nonenzymatic glucose detection using multi-walled carbon nanotube electrodes, Electrochem. Commun. 6 (2004) 66–70, https://doi.org/10.1016/J.ELECOM.2003.10.013.
[36] Y. Bai, Z. Jing, R. Ma, X. Wan, J. Liu, W. Huang, A critical review of enzymes immobilized on chitosan composites: characterization and applications, Bioproc. Biosyst. Eng. 46 (11 46) (2023) 1539–1567, https://doi.org/10.1007/S00449-023-02914-0.
[37] M. Lazouskaya, M. Tamm, O. Scheler, K. Uppuluri, K. Zaraska, Nafion as a protective membrane for screen-printed pH-sensitive ruthenium oxide electrodes. Proceedings of the Biennial Baltic Electronics Conference, BEC 2020-October, 2020, https://doi.org/10.1109/BEC49624.2020.9276822.
[38] J. Lerdsri, J. Upan, J. Jakmunee, Nafion mixed carbon nanotube modified screen-printed carbon electrode as a disposable electrochemical sensor for quantification of Amitraz in honey and longan samples, Electrochim. Acta 410 (2022) 140050, https://doi.org/10.1016/J.ELECTACTA.2022.140050.
[39] M.K. Abraham, A.S. Madanan, S. Varghese, R.S. Lekshmi, A.I. Shkhair, N.S. Vijila, S. George, Fluorescent enzymatic sensor based glucose oxidase modified bovine serum albumin-gold nanoclusters for detection of glucose, Chempluschem 89 (2024) e202300601, https://doi.org/10.1002/CPLU.202300601.
[40] P.R. Miller, S.A. Skoog, T.L. Edwards, D.M. Lopez, D.R. Wheeler, D.C. Arango, X. Xiao, S.M. Brozik, J. Wang, R. Polsky, R.J. Narayan, Multiplexed microneedle-based biosensor array for characterization of metabolic acidosis, Talanta 88 (2012) 739–742, https://doi.org/10.1016/J.TALANTA.2011.11.046.
[41] W. Niamsi, N. Larpant, P.K. Kalambate, V. Primpray, C. Karuwan, N. Rodthongkum, W. Laiwattanapaisal, Paper-based screen-printed ionic-liquid/graphene electrode integrated with prussian blue/MXene nanocomposites enabled electrochemical detection for glucose sensing, Biosensors (Basel) 12 (2022) 852, https://doi.org/10.3390/BIOS12100852/S1.
[42] K.J. Lee, S.S. Jeong, D.H. Roh, D.Y. Kim, H.K. Choi, E.H. Lee, A practical guide to the development of microneedle systems – in clinical trials or on the market, Int. J. Pharm. 573 (2020) 118778, https://doi.org/10.1016/J.IJPHARM.2019.118778.
[43] M. Teodorescu, M. Bercea, S. Morariu, Biomaterials of PVA and PVP in medical and pharmaceutical applications: perspectives and challenges, Biotechnol. Adv. 37 (2019) 109–131, https://doi.org/10.1016/J.BIOTECHADV.2018.11.008.
[44] E.E. Doğan, P. Tokcan, M.E. Diken, B. Yilmaz, B.K. Kizilduman, P. Sabaz, Synthesis, characterization and some biological properties of PVA/PVP/PN hydrogel nanocomposites: antibacterial and biocompatibility, Adv. Mater. Sci. 19 (2019) 32–45, https://doi.org/10.2478/ADMS-2019-0015.
[45] A. Himawan, Q.K. Anjani, U. Detamornrat, L.K. Vora, A.D. Permana, R. Ghanma, Y. Naser, D. Rahmawanty, C.J. Scott, R.F. Donnelly, Multifunctional low temperature-cured PVA/PVP/citric acid-based hydrogel forming microarray patches: physicochemical characteristics and hydrophilic drug interaction, Eur. Polym. J. 186 (2023) 111836, https://doi.org/10.1016/J.EURPOLYMJ.2023.111836.
[46] W.F. Bergfeld, F.A.C.P. Donald, V. Belsito, R.A. Hill, C.D. Klaassen, D.C. Liebler, J. G. Marks, R.C. Shank, T.J. Slaga, P.W. Snyder, Safety assessment of polyvinyl alcohol as used in cosmetics status: reassessment of re-review for panel review release the 2014Cosmetic ingredient review expert panel members are: chairman. www.cir-safety.org, 2014. (Accessed 9 March 2025).
[47] S. Aoyagi, H. Izumi, M. Fukuda, Biodegradable polymer needle with various tip angles and consideration on insertion mechanism of mosquito's proboscis, Sens. Actuators A Phys. 143 (2008) 20–28, https://doi.org/10.1016/J.SNA.2007.06.007.
[48] J. Ling, L. Jiang, K. Chen, C. Pan, Y. Li, W. Yuan, L. Liang, Insertion and pull behavior of worker honeybee stinger, J. Bionic. Eng. 13 (2016) 303–311, https://doi.org/10.1016/S1672-6529(16)60303-7/METRICS.
[49] K.M. Saifullah, A. Mushtaq, P. Azarikhah, P.D. Prewett, G.J. Davies, Z. Faraji Rad, Micro-vibration assisted dual-layer spiral microneedles to rapidly extract dermal interstitial fluid for minimally invasive detection of glucose, Microsyst. Nanosci. 11 (1 11) (2025) 1–18, https://doi.org/10.1038/s41378-024-00850-x.
[50] A.H. Sabri, Z. Cater, J. Ogilvie, D.J. Scurr, M. Marlow, J. Segal, Characterisation of mechanical insertion of commercial microneedles, J. Drug Deliv. Sci. Technol. 58 (2020) 101766, https://doi.org/10.1016/J.JDDST.2020.101766.
[51] FDA Guidance of Micro-Needling Products | RegDesk, (n.d.). https://www.regdesk.co/fda-micro-needling/(accessed March 15, 2025).
[52] Microneedling: Things to consider | Therapeutic Goods Administration (TGA), (n.d.). https://www.tga.gov.au/news/news/microneedling-things-consider (accessed March 15, 2025).